Remote Sensing of Environment 219 (2018) 145–161

Contents lists available at ScienceDirect

Remote Sensing of Environment

journal homepage: www.elsevier.com/locate/rse

The Harmonized Landsat and Sentinel-2 surface reflectance data set

Martin Claverie[a,b,*], Junchang Ju[b,c], Jeffrey G. Masek[b], Jennifer L. Dungan[d], Eric F. Vermote[b], Jean-Claude Roger[a,b], Sergii V. Skakun[a,b], Christopher Justice[a]

[a] Department of Geographical Sciences, University of Maryland, College Park, MD 20742, USA
[b] NASA Goddard Space Flight Center, 8800 Greenbelt Road, Greenbelt, MD 20771, USA
[c] Earth System Science Interdisciplinary Center, University of Maryland, College Park, MD 20740, USA
[d] NASA Ames Research Center, Moffett Field, CA 94035, USA

ARTICLE INFO

Keywords:
Landsat
Sentinel-2
Surface reflectance
Virtual Constellation
Harmonization
Analysis Ready Data

ABSTRACT

The Harmonized Landsat and Sentinel-2 (HLS) project is a NASA initiative aiming to produce a Virtual Constellation (VC) of surface reflectance (SR) data acquired by the Operational Land Imager (OLI) and Multi-Spectral Instrument (MSI) aboard Landsat 8 and Sentinel-2 remote sensing satellites, respectively. The HLS products are based on a set of algorithms to obtain seamless products from both sensors (OLI and MSI): atmospheric correction, cloud and cloud-shadow masking, spatial co-registration and common gridding, bidirectional reflectance distribution function normalization and spectral bandpass adjustment. Three products are derived from the HLS processing chain: (i) S10: full resolution MSI SR at 10 m, 20 m and 60 m spatial resolutions; (ii) S30: a 30 m MSI Nadir BRDF (Bidirectional Reflectance Distribution Function)-Adjusted Reflectance (NBAR); (iii) L30: a 30 m OLI NBAR. All three products are processed for every Level-1 input products from Landsat 8/OLI (L1T) and Sentinel-2/MSI (L1C). As of version 1.3, the HLS data set covers 10.35 million km^2 and spans from first Landsat 8 data (2013); Sentinel-2 data spans from October 2015.

The L30 and S30 show a good consistency with coarse spatial resolution products, in particular MODIS Collection 6 MCD09CMG products (overall deviations do not exceed 11%) that are used as a reference for quality assurance. The spatial co-registration of the HLS is improved compared to original Landsat 8 L1T and Sentinel-2A L1C products, for which misregistration issues between multi-temporal data are known. In particular, the resulting computed circular errors at 90% for the HLS product are 6.2 m and 18.8 m, for S10 and L30 products, respectively. The main known issue of the current data set remains the Sentinel-2 cloud mask with many cloud detection omissions. The cross-comparison with MODIS was used to flag products with most evident non-detected clouds. A time series outlier filtering approach is suggested to detect remaining clouds. Finally, several time series are presented to highlight the high potential of the HLS data set for crop monitoring.

1. Introduction

Many land monitoring applications require more frequent observations than can be obtained from a single “Landsat-class” sensor. Numerous studies have documented the need for higher temporal resolution data to better monitor land cover change (Hansen and Loveland, 2012), agricultural management (e.g., Claverie et al., 2012; Skakun et al., 2017b; Whitcraft et al., 2015a), disaster response (Skakun et al., 2014), water resources (Trinh et al., 2017), and vegetation phenology (Melaas et al., 2013).

All these applications require near-daily imagery at medium spatial resolution. Even year-to-year change detection benefits from frequent data coverage in cloudy areas (Roy et al., 2006). Furthermore, with the advent of free imagery archives (Loveland and Dwyer, 2012; Woodcock et al., 2008; Wulder et al., 2012) and the increased availability of powerful computing environments that rely on parallel processing (e.g., NASA Earth Exchange, Amazon Web Services, Google Cloud Computing) (Gorelick et al., 2017; Shelestov et al., 2017), researchers have developed a new capacity for working with large volumes of time series imagery (Nemani, 2011).

With the increasing number of Earth observation satellites, observations from multiple observatories can be merged to provide improved temporal coverage (Li and Roy, 2017).

Combining data from two or more sensors into a single data set creates a so-called “Virtual Constellation” (VC). The Committee on Earth Observation Satellites (CEOS) has defined a VC as a “set of space

* Corresponding author at: Department of Geographical Sciences, University of Maryland, College Park, MD 20742, USA.
E-mail address: martin.claverie@nasa.gov (M. Claverie).

https://doi.org/10.1016/j.rse.2018.09.002
Received 15 August 2017; Received in revised form 28 August 2018; Accepted 3 September 2018
Available online 14 October 2018
0034-4257/

Table 1
HLS input sensors specifications.

		Landsat 8/OLI-TIRS	Sentinel-2A/MSI	Sentinel-2B/MSI
Launch date		February 11, 2013	June 23, 2015	March 7, 2017
Nominal equatorial crossing time		10:00 a.m.	10:30 a.m.	10:30 a.m.
Spatial resolution		30 m (OLI)/100 m (TIRS)	10 m/20 m/60 m (see spectral bands)	
Swath/field of view		180 km/15°	290 km/20.6°	
Spectral bands (central wavelength)	Ultra blue	443 nm	443 nm (60 m)	
	Visible	482 nm, 561 nm, 655 nm	490 nm (10 m), 560 nm (10 m), 665 nm (10 m)	
	Red edge	–	705 nm (20 m), 740 nm (20 m), 783 nm (20 m)	
	NIR	865 nm	842 nm (10 m), 865 nm (20 m)	
	SWIR	1609 nm, 2201 nm	1610 nm (20 m), 2190 nm (20 m)	
	Cirrus	1373 nm	1375 nm (60 m)	
	Water vapor	–	945 nm (60 m)	
	Thermal	10.9 μm, 12 μm	–	

and ground segment capabilities that operate in a coordinated manner to meet a combined and common set of Earth Observation requirements." However, simply having synergistic sensors on orbit is not sufficient for end users; the data products themselves must also be processed in such a way as to ease preprocessing and analysis burden. This concept has been termed Analysis Ready Data (ARD, Egorov et al., 2018; USGS, 2018): data products that are gridded to a common reference and processed to comparable geophysical parameters regardless of their sensor of origin. Beside ARD, space agencies also support multiple sensors application. As an example, the Multi-Source Land Imaging (MuSLI) projects under the NASA Land-Cover and Land-Use Change program (LCLUC, Justice et al., 2015) aim to develop innovative approaches using multiple sensor data for continental and global products.

USGS/NASA Landsat and European Union Copernicus program Sentinel-2 represent the two flagship programs for medium-resolution land imaging. In this paper, we describe a new Harmonized Landsat and Sentinel-2 (HLS) surface reflectance product, with the necessary radiometric and geometric corrections to provide a single, "stackable" source of near-daily reflectance observations at 30-meter resolution. The HLS products are currently available for test sites around the globe, and should be available for North America in the second half of 2018.

The Landsat program is the longest running enterprise for acquisition of satellite imagery of Earth's land areas (Loveland and Dwyer, 2012). The program started in 1972 with Landsat 1 and the most recent platform, Landsat 8, was launched in 2013. Starting in 1982 with Landsat 4, sensors have been characterized by a 16-day repeat cycle, reflective bands at 30-meter resolution for the visible-shortwave infrared (from 450 nm to 2400 nm) and thermal infrared bands at 120-meter (Landsat 4 and 5), 60-meter (Landsat 7), or 100-meter (Landsat 8) resolution.

In 2015 and 2017, the European Space Agency (ESA) launched two satellites of the Sentinel-2 mission (S-2A and S-2B respectively), the second mission of the Copernicus environmental monitoring program (Drusch et al., 2012). The MSI sensor onboard both satellites provides a spatial resolution of 10 to 60 m depending on the wavelength. The Sentinel-2 constellation provides open-access optical imagery of the global land surface with a 5-day revisit period.

The Harmonized Landsat and Sentinel-2 (HLS) product aims to combine in a single data set the observations of the land surface from the two sensors. Given that Landsat 8/OLI and Sentinel-2/MSI make similar measurements in terms of spectral, spatial and angular characteristics and are both placed in sun-synchronous orbits (Table 1), they are ideal candidates to form a VC and generate multi-sensor ARD products. The characteristics of the HLS product are driven by community needs for intra-annual land monitoring, including monitoring agricultural management and condition (Waldner et al., 2016; Whitcraft et al., 2015b) and vegetation phenology. Of paramount importance has been generating "smooth" spectral time series that accurately record land conditions and minimize temporal noise due to sensor-to-sensor differences in atmospheric correction approach, view geometry or bandpass. Although the two sensing systems are generally similar, the building of a harmonized surface reflectance data set has required efforts to mitigate these differences. Specifically, by "harmonized" we mean that the products are:

- Gridded to a common pixel resolution, map projection, and spatial extent (i.e., tile);
- Atmospherically corrected and cloud masked to surface reflectance using a common radiative transfer algorithm;
- Normalized to a common nadir view geometry via Bi-directional Reflectance Distribution Function (BRDF) estimation;
- Adjusted to represent the response from common spectral bandpasses.

In essence, these products are the building blocks for a "data cube" such that a user may examine any given pixel through time, and treat the near-daily reflectance time series as though it came from a single sensor. In the sections below, we describe the HLS product specifications, detail the algorithms of the current data set version (v1.3) used in the processing chain, and give results on data set quality and reflectance uncertainty. The HLS v1.3 data set was processed at the NASA Earth Exchange (NEX, NASA Ames Research Center) which has capacity for working with large volumes of data (Nemani, 2011).

2. Input/output product definition and specifications

2.1. Landsat 8 and Sentinel-2 Level-1 input products

The Operational Land Imager (OLI) sensor is a medium spatial resolution multi-spectral imager onboard the Landsat 8 satellite, in a sun-synchronous orbit (705 km altitude) with a 16-day repeat cycle. The sensor has a field of view of 15 degrees (approximately 185 km). The OLI sensor has 9 bands (Table 1) and is co-registered with the TIRS (Thermal Infrared Sensor) sensor which has two spectral bands. The ground sampling distance for OLI is 30 m and for TIRS is 100 m. The 12 μm TIRS band (band 11) has been significantly affected by stray light which compromises its utility for split-window atmospheric correction (Montanaro et al., 2014).

Standard top-of-atmosphere Landsat 8 products (i.e., Level-1) are distributed by USGS EROS. The highest quality Level-1 product had been labeled L1T, which is radiometrically calibrated and orthorectified using ground control points and digital elevation model data. Starting in 2016, USGS organized the Landsat data archive into a tiered data Collection structure to maintain consistent data quality for time series analysis, and a reprocessing of the global Landsat archive into Collection-1 data was finished in early 2017. The current version of the HLS data set (v1.3) is based on the pre-Collection Landsat 8 L1T data,

which are equivalent to the best quality Tier-1 data in the Collection-based archive. Landsat data are spatially referenced using the World Reference System-2 (WRS-2) and provided in the UTM projection. Multi-temporal Landsat 8 data are co-registered with an accuracy of 6.6 m in the x and y directions (Circular Error 90%, CE90, Storey et al., 2014). However, it has been shown recently that the absolute geodetic registration of Landsat 8 data to the Earth's surface is not optimal due to inaccuracies in the Global Land Survey (GLS) 2000 ground control, which can result in a misregistration of 38 m (2σ) relative to Sentinel-2 imagery in some parts of the globe (Storey et al., 2016). The USGS is planning in the near future to update the GLS ground control to improve the absolute registration accuracy.

The Sentinel-2 Multi-Spectral Instrument (MSI) is onboard the Sentinel-2A and -2B satellites orbiting the Earth at 786 km altitude (Martimort et al., 2007). The ground sampling distance varies among the spectral bands: 10 m for the visible and the broad NIR bands, 20 m for the red edge, narrow NIR and SWIR bands, and 60 m for the atmospheric bands. The sensor has a 20.6° field of view corresponding to an image swath width of approximately 290 km.

Standard Sentinel-2 L1C data are distributed by the ESA Open Access Hub. L1C data are framed into tiles (also named granules) measuring 109.8 km by 109.8 km in the UTM-based Military Grid Reference System (MGRS, ESA, 2015). Adjacent tiles in the same UTM zone overlap in x and y axis predominantly by 9780 m. At the border between two adjacent UTM zones, a tile of one UTM zone can extend into the other UTM zone, overlapping with the tile of the other UTM zone (https://sentinels.copernicus.eu/web/sentinel/user-guides/sentinel-2-msi). In the future, geographic registration will be performed using the Global Reference Image (GRI, Dechoz et al., 2015). The GRI is a database made of MSI mono-spectral images that serves as geographic reference for registering all MSI data. The processing of the GRI was initiated during the commissioning phase and is planned to be completed within the next year (F. Gascon, personal communication, July 2018). The geolocation performance specification for Sentinel-2A is 12.5 m (3σ, Gascon et al., 2017; Languille et al., 2015). From the commissioning phase, ESA has delivered MSI L1C products in several processing baselines (versions) over time. Particularly L1C data processed before version 02.04 did not correctly account for spacecraft yaw angle (ESA, 2018), resulting in misregistration in the overlap regions at the edges of adjacent swaths (Yan et al., 2018). The processing baseline 02.04 introduced in May 2016 implemented an improved yaw angle bias correction. As of 2017, not all the data acquired before May 2016 have been reprocessed to version 02.04, and the most recent processing baseline 02.05 introduced in April 2017 is used mostly for forward processing. Starting in 2018, ESA will systematically improve the capacity of performing the multi-temporal co-registration by registering MSI data to the GRI covering the whole globe with highly accurate geolocation information obtained through a spatio-triangulation algorithm using reference ground control points (Gascon et al., 2017).

2.2. HLS products

At the current stage of development, the HLS data set is comprised of three types of products. All products are gridded into the Sentinel-2 tiling system (MGRS), which is in the UTM/WGS84 projection, with a tile size of 109.8 × 109.8 km. The three types of products are named S10, S30, and L30 (Table 2).

Table 2
HLS Products specifications.

Product name	S10	S30	L30
Spatial	Same as Sentinel-2 L1C	30 m	30 m
Spectral	Same as Sentinel-2 L1C	OLI-like and red-edge bands	OLI and TIRS
Temporal	Same as Sentinel-2 L1C	As input	As input
SR/NBAR	SR	NBAR	NBAR

The S10 product is atmospherically corrected, full spatial-resolution Sentinel-2 MSI surface reflectance. The geolocation of the images in processing baselines prior to 02.04 was adjusted slightly for better co-registration to a reference image per tile of minimal cloud cover from processing base 02.04. No other correction is applied, and the full spatial resolution (i.e. 10 m, 20 m, and 60 m) of the individual MSI bands is preserved. The product is intended for users requiring both the full spatial resolution of Sentinel-2 and the same 6S atmospheric correction approach used operationally for Landsat 8/OLI.

The S30 and L30 products provide 30 m Nadir BRDF-Adjusted Reflectance (NBAR) derived from MSI and OLI data, respectively. The S30 products are derived from S10 products and resampled to 30 m, BRDF-normalized using a fixed solar angle and nadir view, and spectrally adjusted to match Landsat 8/OLI spectral bandpasses. The L30 products are derived from Landsat 8/OLI SR products, and resampled and gridded to the same reference images and MGRS grid used for S30, and BRDF-normalized in the same way as S30.

3. Algorithms

3.1. Overview of HLS processing flow

Our approach to harmonization involves radiometric and geometric adjustments to make a consistent surface reflectance record for time series applications. As such, it is not always possible to preserve the unique features of each data source, and some compromises must be made. We have made the following decisions regarding harmonization:

- The Seninel-2 (S2)/MSI radiometry is adjusted to replicate the spectral bandpasses of Landsat 8/OLI for the bands common to both sensors. For unique bands (i.e., the MSI red edge) and for atmospheric bands (i.e., cirrus and water vapor), no spectral adjustment is performed.
- The harmonized products (S30, L30) are gridded to a common 30 m resolution. Although this degrades the MSI 10 m and 20 m resolution, it provides consistency with the Landsat archive. In addition, a key goal of the project is to generate consistent time series observations. Super-sampling OLI observations to 10 m, in order to obtain a harmonized products at 10 m, would introduce temporal noise simply due to the spatial averaging inherent to the coarser data product.
- The harmonized products are gridded to a common UTM projection and spatial extent, based on the Sentinel-2 tiling system. Although other tiling systems are in use (e.g. the MODIS/WELD sinusoidal system, Roy et al., 2010), sinusoidal projections are problematic for areas far from the central meridian, and the UTM-based Sentinel-2 system provides a reasonable approach for local-scale data presentation.

The HLS processing chain is structured in four processing steps (Fig. 1). The processing algorithms reflect the state-of-the-art medium resolution optical remote sensing data processing techniques. Atmospheric correction of satellite imagery to surface reflectance has now become a standard practice, and forms the basis for the CEOS Analysis Ready Data for Land (CARD4L) standard (CEOS, 2016). In addition, that Sentinel-2 and Landsat 8 have different orbit and view geometries necessitates normalization to a fixed view and solar angle via BRDF modeling.

3.2. Atmospheric correction

The atmospheric correction method is based on the Land Surface Reflectance Code (LaSRC), an algorithm primarily developed for

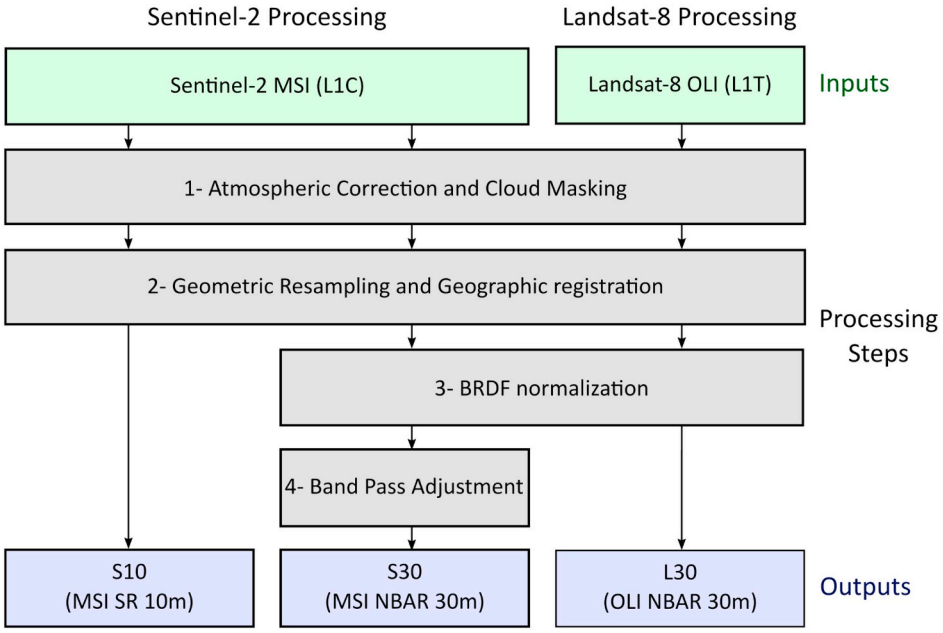

Fig. 1. Overview of the HLS processing. The four processing steps are colored in grey.

operational use with Landsat 8 imagery (Vermote et al., 2016) and further extended for Sentinel-2 (Doxani et al., 2018). LaSRC is based on heritage from the MODIS MCD09 products (Vermote and Kotchenova, 2008) as well as the earlier LEDAPS algorithm implemented for Landsat-5 and -7 (Masek et al., 2006). In brief, LaSRC assumes a Lambertian, plane-parallel atmosphere, and uses the 6S radiative transfer model (Kotchenova and Vermote, 2007) to invert directional surface spectral reflectance from observed top-of-atmosphere reflectance. The retrieval accounts for both molecular and particle scattering, as well as absorption by water vapor and ozone. Several atmospheric parameters are required for the inversion including surface pressure (from the National Center for Environmental Prediction Global Data Assimilation System – NCEP GDAS weather model), column water vapor (derived from the MODIS near-infrared channels), ozone (from NCEP GDAS), and aerosol properties (aerosol optical thickness and Angstrom exponent). Of these, aerosol optical thickness (AOT) is the most challenging due to its strong influence on shorter wavelength channels, and degree of local variability. Because of this local variability, image-based approaches to retrieving aerosol are preferred. Like the current MODIS Collection 6 algorithm, the LaSRC algorithm assumes two SR ratios, red to blue and red to ultra blue, and uses the difference between these assumed ratios and observed TOA reflectance ratios to invert for AOT and Angstrom exponent. The two fixed SR ratios for the globe are derived from MODIS and MISR data, and expressed as a function of mid-infrared vegetation index, as described in Vermote et al. (2016). Adjacency effects are not corrected.

Uncertainty estimates for LaSRC are based on comparison with corrections based on in situ atmospheric parameters from the Aerosol Robotic Network (AERONET, Vermote et al., 2016). These comparisons indicate improved performance compared to the LEDAPS algorithm or an alternative version of LEDAPS that used MODIS aerosol products as input (Ju et al., 2012). For Landsat 8 OLI, overall uncertainty varied from 0.11% absolute reflectance (SWIR1 band) to 0.85% absolute reflectance (blue band). HLS uses the Landsat 8 LaSRC algorithm directly for atmospheric correction of Landsat 8 products. A separate version of LaSRC has been prepared for the use with Sentinel-2/MSI imagery, incorporating pre-launch measurements of the MSI spectral bandpasses. Validation of the LaSRC algorithm for both Landsat 8 and Sentinel-2 was undertaken within the Atmospheric Correction Inter-comparison eXercise (ACIX) which is an international initiative to analyze the surface reflectance (SR) products of various state-of-the-art atmospheric correction (AC) processors (Doxani et al., 2018). For Sentinel-2/MSI, overall uncertainty varied from 0.3% absolute reflectance (SWIR1 band) to 1.4% absolute reflectance (blue band).

For both Landsat 8 OLI and Sentinel-2/MSI, an internal version 3.5.5 of the LaSRC was used.

3.3. Cloud and related masks

Most time series applications of optical satellite data require an accurate cloud and shadow mask. For L30, we selected the cloud mask generated by the LaSRC processor, which has shown good performance (Foga et al., 2017, 4.7% of cloud omission and 24% of cloud commission). The lack of a thermal infrared band on Sentinel-2 presents a challenge, since cloud tops can be accurately detected via temperature difference compared to surrounding land areas. Many Sentinel-2 processors have been developed for cloud detection (e.g., Hagolle et al., 2010; Louis et al., 2016), but have not yet been fully validated or compared to other algorithms. We selected the adaptation of Fmask for Sentinel-2 S10 and S30 products (Zhu et al., 2015) relying on the long-term performance of Fmask with Landsat data (Zhu and Woodcock, 2012, 2014).

3.3.1. LaSRC for Landsat 8

The cloud mask in the LaSRC atmospheric correction module applied to Landsat 8 OLI imagery is defined using thresholds for the following components: (i) the residual from the AOT inversion based on the two ratios (red vs blue and red vs ultra blue, see Section 2.2) with threshold 0.05, (ii) the brightness temperature retrieved from TIRS band 1 with threshold 305 K. Adjacency cloud is applied over 150 m windows (i.e., five 30 m pixels with the window size selected empirically) surrounding cloudy pixels. Cloud shadows are determined based on: (i) the cloud location, (ii) an a priori cloud height range using TIRS band 10 with an uncertainty of ± 1 km (Vermote and Saleous, 2007), (iii) the TOA reflectance in band 6, and (iv) the difference between TOA reflectances in band 4 and 3. Positive Normalized Difference Snow Index (NDSI) pixels are flagged as snow (Hall et al., 2002). This low threshold for NDSI was selected empirically.

3.3.2. Fmask for Sentinel-2

Fmask is an automated cloud, cloud shadow, and snow detection algorithm initially developed for Landsat data (Zhu and Woodcock,

2012, 2014). Fmask is based on a set of TOA reflectance thresholds to classify clouds, cloud shadows, water and snow. The Fmask algorithm relies on cloud and cloud shadow matching using sun-view geometry information. Since it is initially designed for Landsat data, the algorithm relies on thermal data. However, recently, (Zhu et al., 2015) published an adapted version of Fmask to work in different configurations with options to omit thermal and/or cirrus bands. The Sentinel-2 algorithm is, therefore, based on the Fmask version using the cirrus band and without the thermal one. The per-pixel sun-view geometry information is derived from the L1C metadata. The Sentinel-2 Fmask code is available here: https://github.com/prs021/fmask.

3.4. Spatial co-registration and gridding

Image registration accuracy can be separated into two components. Absolute geodetic accuracy refers to the accuracy of image registration relative to ground reference. Multi-temporal registration accuracy refers to the accuracy of co-registration among multiple image acquisitions throughout the time. Our objective in HLS is to maintain the geodetic accuracy requirement of the Sentinel-2 images (< 20 m error, 2σ) and improve the multi-temporal co-registration among Sentinel-2 images and between Sentinel-2 and Landsat 8 images (< 15 m 2σ) for the 30 m products. This specification supports time series monitoring of small fields, man-made features, and other spatially heterogeneous cover types.

Two issues impede our ability to directly register Landsat 8 and Sentinel-2 imagery without additional processing. First, while the relative co-registration of Landsat 8/OLI imagery is quite accurate (< 6.6 m, Storey et al., 2014), the absolute geodetic accuracy varies with the quality of the Global Land Survey 2000 (GLS2000) ground control around the world. In some locations, the GLS geodetic accuracy can be in error by up to 38 m (2σ, Storey et al., 2016). As a result, Sentinel-2/MSI and Landsat 8/OLI Level-1 products may not align to sub-pixel precision for those locations (Storey et al., 2016). Second, an error in the yaw characterization for the MSI L1C images processed before v02.04 (May 2016) caused misregistration between the edges of MSI images acquired from adjacent orbits (ESA, 2018). The misregistration of up to 2.8 pixels at 10 m resolution between Sentinel-2A images from adjacent orbits has been observed by Skakun et al. (2017a) and Yan et al. (2018). Although the issue was fixed with L1C version 02.04 (yielding to a measured absolute geolocation of < 11 m at 95.5% confidence, ESA, 2018), archived data from 2015 to 2016 will continue to have this error until the entire archive is reprocessed by ESA.

ESA is planning to release a Global Reference Image (GRI) composed of the most accurately registered MSI imagery for the globe to register all the archived and new MSI images. USGS will use the GRI ground control points to improve the GLS2000 ground control, thus bringing Landsat and Sentinel-2 Level-1 products into alignment (Storey et al., 2016). Since the GRI set has not been used in ESA L1C data production yet, we selected for each HLS tile our own reference image, an MSI image of processing L1C baseline version 02.04 with minimal cloud cover. MSI images were selected as reference since MSI absolute geodetic accuracy is better than OLI (Storey et al., 2014, 2016). Then we used the Automated Registration and Orthorectification Package (AROP, Gao et al., 2009), to align all Landsat 8 and pre-v02.04 MSI imagery to the reference image of each tile. The NIR band (B5 for OLI and B8A for MSI) was used by AROP in the cross-correlation analysis to identify tie points.

AROP is parameterized to produce a system of linear equations, based on a large number of tie points derived from cross-correlation of small areas (Eq. (1)).

$$\begin{cases} x' = a_1 + a_2 x + a_3 y \\ y' = b_1 + b_2 x + b_3 y \end{cases} \quad (1)$$

where (x, y) and (x', y') correspond to the pixel coordinates of the reference (Sentinel-2 base image) and the warped image (Sentinel-2 or Landsat 8 image), respectively, and a_1, a_2, a_3 and b_1, b_2, b_3 are the AROP coefficients estimated using ordinary least squares (Gao et al., 2009).

Cloudy areas will generally result in low correlation coefficients for the local area and the potential tie point is excluded from the solution. If the entire image is cloudy, the overall polynomial fit will be poor, or there will not be sufficient valid tie points (< 10) across the image. In those cases an HDF metadata flag is set to indicate that co-registration and resampling were not performed.

The Landsat-8 surface reflectance is resampled using cubic convolution interpolation for the AROP-derived coordinate transformation. Note that if any of the pixels in the 4 × 4 interpolation kernel contains fill value, the output will be a fill value; this resultant loss of data ensures the overall data integrity. The QA bits resampling is tricky since the QA bits are categorical data and the pixels in the 4 × 4 interpolation kernel are not equally important. Therefore, we arbitrarily consider only the inner 2 × 2 pixels, which carry predominant weights over the outer pixels in the cubic convolution interpolation of surface reflectance, and apply a "presence" rule: if a QA bit is set to 1 for any of the inner 2 × 2 pixels, the output QA bit will be set to 1. This aggressiveness in QA resampling avoids introduction of new cloud masking omission errors.

Similarly, the coordinates of version 02.00–03 L1C based Sentinel-2 surface reflectance are adjusted with the use of AROP, and the surface reflectance in the 10 m, 20 m, and 60 m bands and the QA band are resampled in the Landsat-8 way. In contrast, coordinate adjustment and data resampling are not needed for surface reflectance from version 02.04 or later L1C input. The output product is S10.

The 30 m Sentinel-2 surface reflectance is derived from S10, by resampling all S10 bands to 30 m. The 10 m pixels are resampled to 30 m by averaging the nine 10 m values within a 30 m square. The 20 m bands are resampled to 30 m by averaging with area-based weights 4/9, 2/9, 2/9, and 1/9 for the four 20 m pixels overlapping the intended 30 m pixel. The reflectance of a 60 m pixel is replicated to the four intended 30 m pixel locations. The S10 QA band is available at 10 m, and its resampling to 30 m is straightforward with the same "presence" rule described earlier.

3.5. View and illumination angles (BRDF) adjustment

Given the differing solar and view angles associated with Landsat 8 and Sentinel-2, normalizing the BRDF effects is desirable. Retrieving the BRDF information directly from medium resolution optical remote sensing data is not feasible with the current temporal and angular distribution of the data. Instead, the BRDF information needs to be ingested as a priori. Many techniques rely on the MCD43 MODIS moderate resolution BRDF product (e.g., Claverie et al., 2015a; Franch et al., 2014; Gao et al., 2014; Roy et al., 2008). However, these techniques may generate artefacts due to the spatial resolution differences. Recently, Claverie et al. (2015a) and Roy et al. (2016) found that a single, global and constant BRDF shape produces satisfying BRDF normalization over a limited range of view zenith angles near nadir. We selected the c-factor technique and global coefficients provided by Roy et al. (2016) because the technique is very stable, reversible, easy to implement for operational processing and has been evaluated for Sentinel-2 data (Roy et al., 2017).

The c-factor technique uses fixed BRDF coefficients for each spectral band, i.e., a constant BRDF shape, derived from a large number of pixels in the MODIS 500 m BRDF product (MCD43) that are globally and temporally distributed (> 15 billion pixels). The technique has been evaluated using ETM+ data off-nadir (i.e. on the overlap areas of adjacent swaths, Roy et al., 2016) and MSI data (Roy et al., 2017). The technique is applied in HLS on OLI and MSI bands equivalent to MODIS ones; MSI red-edge spectral bands are therefore not normalized. Normalized reflectance is calculated for original reflectance and a c-factor (Eq. (2)). The latter is deduced (Eq. (3)) from BRDF coefficients for the

Table 3
BRDF coefficients used for the c-factor technique (Roy et al., 2016).

MODIS band	f_{iso}	f_{geo}	f_{vol}
1 (red)	0.169	0.0227	0.0574
2 (NIR)	0.3093	0.033	0.1535
3 (blue)	0.0774	0.0079	0.0372
4 (green)	0.1306	0.0178	0.058
6 (1.6 μm)	0.343	0.0453	0.1154
7 (2.1 μm)	0.2658	0.0387	0.0639

three kernels (isotropic, volumetric and geometric, Table 3). The kernel definitions are described in the ATBD of the MOD43 product (Strahler et al., 1999).

$$\rho(\lambda, \theta^{Norm}) = c(\lambda) \times \rho(\lambda, \theta^{sensor}) \quad (2)$$

$$c(\lambda) = \frac{f_{iso}(\lambda) + f_{geo}(\lambda) \times K_{geo}(\theta^{Norm}) + f_{vol}(\lambda) \times K_{vol}(\theta^{Norm})}{f_{iso}(\lambda) + f_{geo}(\lambda) \times K_{geo}(\theta^{sensor}) + f_{vol}(\lambda) \times K_{vol}(\theta^{sensor})} \quad (3)$$

where θ^{Sensor} refers to the sun-illumination geometry configuration (i.e., Θ_v, Θ_s, $\Delta\phi$) of the input data and θ^{Norm} refers to the sun-illumination geometry configuration of the normalized data ($\theta_v = 0, \theta_s = \theta_s^{out}, \Delta\varphi = 0$).

The S30 and L30 reflectance products are normalized for per-pixel view and per-tile illumination angles. This normalization is applied to all S30 and L30 optical bands except the MSI red-edge bands and the cirrus and water vapor bands for which no MODIS BRDF information is available. The view angle is set to nadir and the solar zenith angle is fixed through time but varies for each tile based on the latitude.

OLI and MSI equator crossing times are close: 10:00 AM and 10:30 AM, respectively. A 6th degree polynomial as a function of the latitude was used to retrieve a constant the solar zenith angle (SZA) per location, named θ_s^{out}. The approach is similar to Zhang et al. (2016), who derived the time of acquisition from a 6th degree polynomial, yielding to a seasonal variation of SZA. In the HLS products, the use of a constant SZA through time is employed in order to monitor temporal changes due to actual land surface temporal changes. The polynomial was fitted based on the entire Landsat 8 archive (Fig. 2). A single θ_s^{out} value per tile is defined based on the tile central latitude and Eq. (4) (where k_i values are given in Fig. 2). Consequently, the output SZA for S30 and L30 products varies latitudinally for the tile center but not temporally.

$$\theta_s^{out} = \sum_{i=0}^{6} k_i \times Lat^i \quad (4)$$

3.6. Bandpass adjustment

The harmonization also requires adjustment of the small differences between the equivalent spectral bands of MSI and OLI. The OLI spectral bandpasses are used as reference, to which the MSI spectral bands are adjusted. No bandpass adjustment is defined for the (i) MSI red-edge bands (B05, B06 and B07), (ii) broad NIR band (B08), and (iii) atmospheric bands (B09 and B10). Note that the HLS v1.3 dataset discussed here relies on the MSI Relative Spectral Response (RSR) v2.0. ESA subsequently issued corrections to the RSR functions for bands 1 and 2 for Sentinel-2a. HLS version 1.4, slated for release in 2018, will update the RSR functions for these bands.

The bandpass adjustment algorithm was derived from a selection of Hyperion spectra. The Hyperion sensor on Earth Observing-1 has collected > 11,000 hyperspectral images since its launch in 2001 (Middleton et al., 2013). The archive is a unique source for building biome-specific spectra libraries using actual observed conditions around the world. Hyperion acquires images in 220 unique spectral bands ranging from 357 nm to 2.576 μm with a 10 nm bandwidth. The instrument operates in a push-broom configuration, with a spatial resolution of 30 m for all bands and a 7.7 km swath.

The Hyperion scenes were selected for each band of latitude (10° width, from −50° to +60°) by choosing one scene, with a "0 to 9% Cloud Cover" assigned in the metadata, per latitude band and per dominant biome type. The IGBP (International Geosphere Biosphere Programme) land cover map (Hansen et al., 1998) was used to quantify the percentage of coverage for each of the 17 IGBP biome types and to select the scenes with highest biome type coverage. This yielded a total of 187 combinations (11 latitude bands × 17 biome types). However, because of the absence of the "Deciduous Needle Leaf Forest" and the "Snow & Ice" classes on tropical latitudes, a total of 158 scenes were selected (Fig. 3).

We used radiometrically and geometrically calibrated Level 1T at-sensor radiance Hyperion data as input. Spectral bands flagged as non-calibrated were removed from the analysis. The data were then atmospherically corrected using the 6S model (Second Simulation of the Satellite Signal in the Solar Spectrum), supplied with aerosol optical thickness (AOT), water vapor, and ozone content included in the MODIS Terra Climate Modeling Grid (CMG - 0.05° spatial resolution) surface reflectance product (MOD09CMG). This assumed a relative stability of the atmosphere, knowing that the acquisition time of the two systems can be apart by 1 h. For each CMG pixel, 6S coefficients were retrieved using MODIS Terra ancillary data at 0.05° and mapped at 30 m to retrieve surface reflectance from Hyperion top of atmosphere radiance.

The 158 selected scenes provided a total of 160 million pixels. To reduce the size of the data set while maintaining the largest variability of spectra, we applied the following processing:

- For each scene, a Principal Components Analysis (PCA) was performed on the surface reflectance data.
- An unsupervised k-means classifier was run on each scene using the

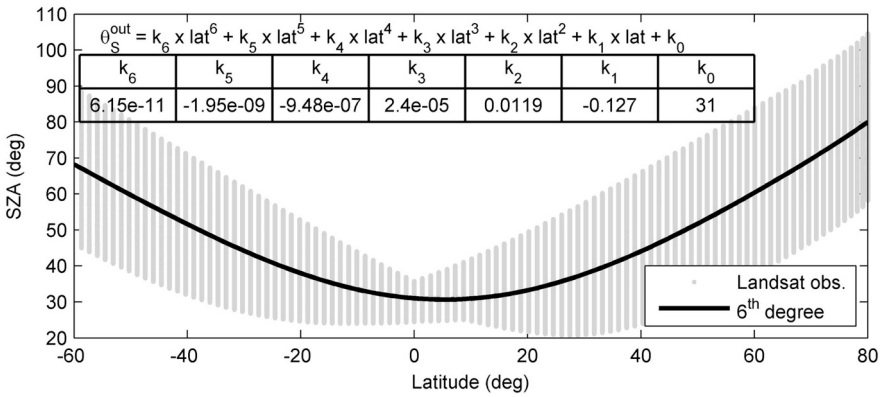

Fig. 2. Solar zenith angle (SZA) and central latitude of all the scenes in the Landsat 8 archive. The line corresponds to the overall fit using a 6th degree polynomial.

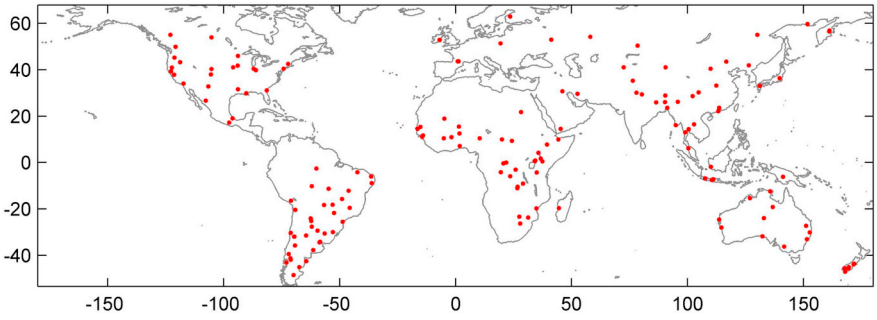

Fig. 3. Map of 160 Hyperion scenes, used to define the hyperspectral data set.

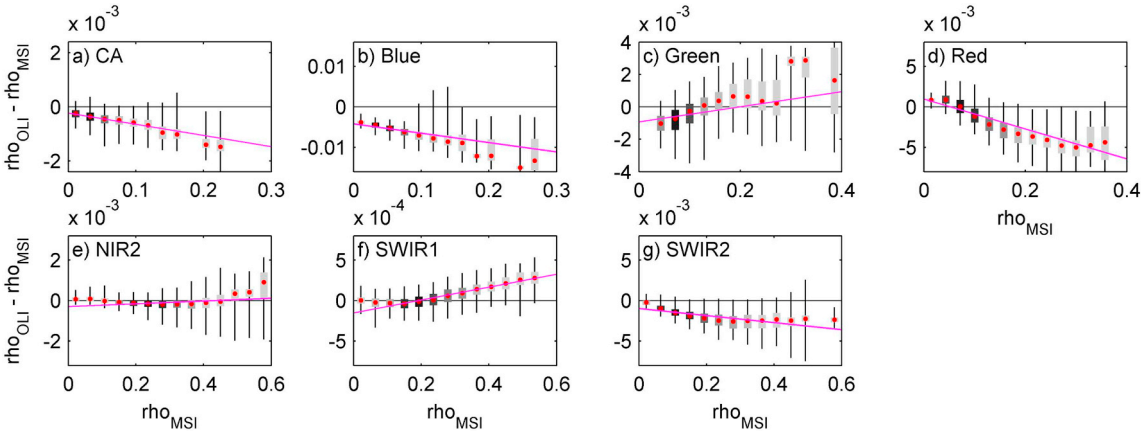

Fig. 4. Boxplots of the differences between simulated MSI and OLI SR using a 0.02 unit bin. The color of the boxplot reflects the density of the distribution (light grey = low density; black = high density) and the red dots the medians. The magenta lines correspond to the bandpass adjustment fits (Table 4). (For interpretation of the references to color in this figure legend, the reader is referred to the web version of this article.)

PCA coefficients accounting for 99% of the variance. The number of output classes ranged from 4 to 343 (median was 99), depending on the size of the scene and on the surface heterogeneity.

- The centroid spectra of each class were identified (i.e., full spectra and also geographic coordinates).

More than 16,000 centroid spectra were retrieved from the 158 scenes. A second clustering was applied to merge the data set (i.e., spectra derived from all scenes combined) to reduce the number of spectra to 10,000; the same PCA and k-means methods were used. The Hyperion spectra data set thus includes 10,000 spectra corresponding to 10,000 Hyperion observations.

The Fig. 4 displays differences between the simulated MSI and OLI surface reflectance values simulated from the Hyperion data set and the derived regression line. A simple least squares linear regression between equivalent spectral bands from MSI (explanatory variable) and OLI (dependent variable) reflectance was used, as in Teillet et al. (2007). The regression coefficients (Table 4) were derived from MSI and OLI reflectance simulated from the 10,000 hyperspectral reflectance spectra. The S30 products were derived using these calibrated linear regressions. The coefficients differ from the ones retrieved by Zhang et al. (2018). These authors used real observations from both sensors (at Toa or NBAR level), implying various atmospheric and geometric conditions, whereas the coefficients retrieved in Table 4 were computed from the same Hyperion spectra convoluted with MSI and OLI RSR.

Table 4
Coefficients of the linear regression bandpass adjustment (OLI = slope × MSI + OLI) and the mean residual.

Band name	Slope	Offset	Residual
Ultra blue	0.996	−0.00023	0.0004
Blue	0.977	−0.00411	0.0018
Green	1.005	−0.00093	0.0011
Red	0.982	0.00094	0.0015
NIR	1.001	−0.00029	0.0003
SWIR 1	1.001	−0.00015	0.0001
SWIR 2	0.996	−0.00097	0.0009

4. Overview of the HLS data set

4.1. The HLS data set

As of version 1.3, HLS products have been produced over 91 regions or test sites, corresponding to a total of 1047 MGRS tiles covering 10.36 million km^2 (Fig. 5). Current sites include, for instance, large regions (West India, South-East Australia, South Africa, Tanzania, Germany), small regions (e.g., Everglades, Belgium), and single MGRS tiles (e.g., Aeronet sites). Of these, 23 regions were selected to support the MuSLI science team for a range of applications (e.g., phenology, fire monitoring, crop and forest monitoring). Fourteen sites were selected for validation purposes; they include Aerosol Robotic Network, Fluxnet, Southern African Regional Science Initiative Project, and Baseline Surface Radiation Network sites where aerosols or surface radiance measurements are available. Finally, five sites over agricultural regions were selected to support the GEOGLAM (GEO Global Agricultural Monitoring) initiative (Becker-Reshef et al., 2010; Whitcraft et al., 2015a); three of them are part of the JECAM (Joint Experiment for Crop Assessment and Monitoring) network (Waldner et al., 2016).

The temporal coverage of the HLS data set starts with the Landsat 8 OLI products in April 2013 (Landsat 8 launch) and Sentinel-2A/MSI products in October 2015 (Sentinel-2A end of commissioning period). It uses all the L1T and the best-quality MSI L1C products of good quality

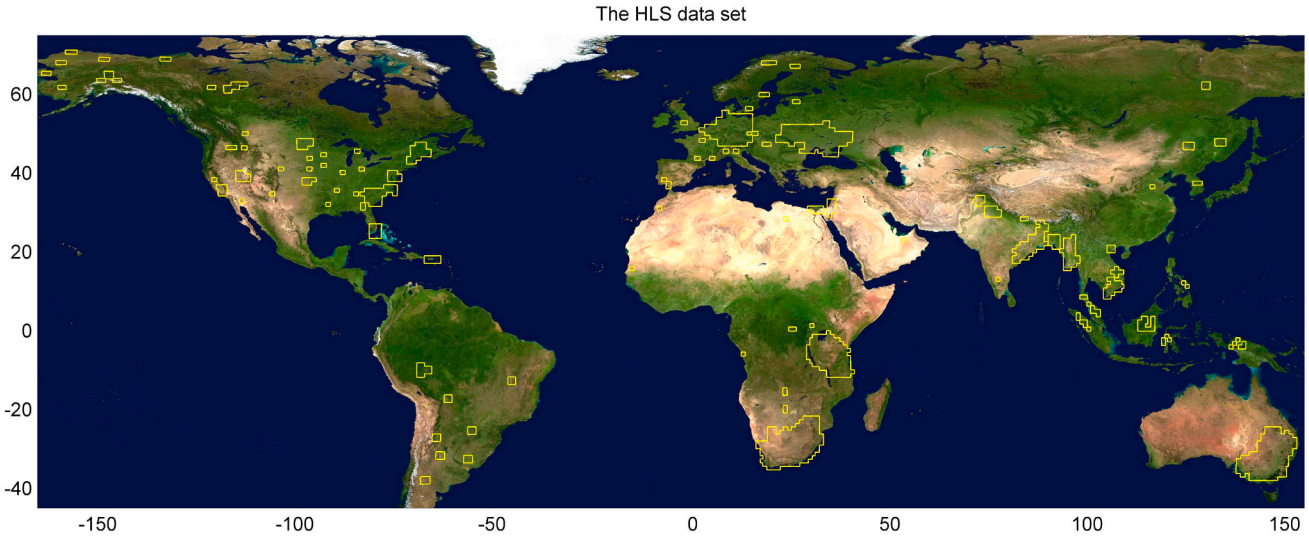

Fig. 5. The HLS test sites as of v1.3, illustrated in 1047 MGRS tiles (adjacent tiles were merged), over the MODIS-derived global green vegetation map (NASA). (For interpretation of the references to color in this figure legend, the reader is referred to the web version of this article.)

(with quality flag "PASSED" for all categories in the metadata) available for the selected MGRS tiles, including overlapping data from adjacent swaths. The lag from satellite image acquisition to HLS product creation is between 2 and 10 days, depending mostly on the availability of ancillary data for atmospheric correction. The v1.3 data set accounts for 68,878 S10/S30 products and 165,083 L30 products. Table 5 summarizes the geographic and temporal distribution of the HLS products. Europe is the best represented continent, as it was prioritized in the Sentinel-2 acquisition plan.

4.2. Time series density

Landsat 8 has a revisit cycle of 16 days, meaning each part of Earth is observed every 16 days with the same view angle. For the Sentinel-2A and 2B, the revisit cycles are both 10 days. Swath overlap between adjacent orbits implies that some areas are observed from more than one orbit per revisit cycle, and this overlap increases with latitude. Therefore, it is important to use all potential observations from all orbit tracks to create a denser time series. Sensor swath footprints of Sentinel-2A and Landsat-8 were calculated based on two-line-element data set (www.space-track.org), assuming (i) 15° and 20.6° cross-track field of view for OLI and MSI, respectively, (ii) a nadir view and (iii) a full acquisition strategy over land. Sentinel-2B results were considered equal to Sentinel-2A ones. Fig. 6-a shows the overlap percentage (percentage of the swath width observed by two or more orbits for each repeat cycle) for each sensor as a function of latitude during each sensor's revisit cycle. Landsat 8 (L8) has a slightly larger overlap (by ~5%) at all latitudes than Sentinel-2 (S2); this is explained by the fact that numbers are expressed in percentages of overlapped area. However, accounting for the difference of orbit cycles (Fig. 6-b), the mean S2 revisit is ~35% higher than L8. The combination of L8 and S-2A allows a theoretical revisit period of 5.7 days at the equator and as short as 3.2 days around the 55° latitude. The use of L8 in addition to the S2 constellation provides a theoretical revisit period of 5.7 days at the equator and as short as 3.2 days around the 55° latitude (numbers in accordance with, Li and Roy, 2017), meaning a decrease of the revisit period by 25% on average as compared as the use of the S2 constellation only.

5. Product evaluation

The creation of a long-term surface reflectance data record requires the development and implementation of Quality Assessment (QA) methods (Roy et al., 2002) to verify the quality of the product. A primary QA data layer is included in the HLS product to flag for each pixel the presence of cloud, cirrus, cloud-shadow, water or with a high aerosol flag. In order to mitigate confusion, product evaluation is referred, hereafter, to Quality Control (QC). QC is an integral part of the HLS production chain. The validation of the SR reflectance products represents the main source of uncertainty. The latter has been evaluated for the OLI products (Vermote et al., 2016) and on-going research is performed for MSI. In this paper, a theoretical uncertainty budget is

Table 5
Number in thousands of L30 and S30 (or S10) products of the v1.3 HLS data set, categorized in continents and quarters.

		2013				2014				2015				2016				2017		Σ
		Q1	Q2	Q3	Q4	Q1	Q2	Q3	Q4	Q1	Q2	Q3	Q4	Q1	Q2	Q3	Q4	Q1	Q2	
Europe	S30												2.0	3.3	4.2	4.5	4.6	4.3	4.3	27.1
	L30	< 0.1	2.6	3.2	3.1	3.0	3.2	3.4	3.4	3.1	3.4	3.4	3.4	3.3	3.3	3.4	3.4	3.3	1.2	53.0
Africa	S30												0.8	1.0	1.6	1.8	1.9	1.9	1.8	10.7
	L30	< 0.1	1.6	2.0	1.8	1.9	2.0	2.0	1.9	1.8	2.0	2.0	1.9	1.9	2.0	2.0	1.9	1.9	0.7	31.2
Asia	S30												0.6	1.1	1.6	1.8	2.3	1.9	1.8	11.0
	L30	< 0.1	1.5	1.9	1.9	1.9	2.0	2.1	2.0	1.9	2.0	2.1	2.0	2.0	2.1	2.0	2.1	2.0	0.7	32.3
Australia &	S30												0.7	0.9	1.4	1.4	1.9	1.6	1.5	9.4
Oceania	L30	< 0.1	1.3	1.7	1.5	1.5	1.7	1.7	1.7	1.6	1.7	1.7	1.7	1.7	1.8	1.7	1.8	1.7	0.6	27.1
America	S30												0.9	1.4	1.7	1.8	1.7	1.6	1.7	10.7
	L30	< 0.1	1.0	1.3	1.2	1.1	1.3	1.4	1.3	1.3	1.4	1.4	1.4	1.4	1.4	1.4	1.3	1.3	0.5	21.5
Global	S30												4.9	7.6	10.4	11.4	12.4	11.3	10.9	68.9
	L30	0.3	7.9	10.1	9.4	9.5	10.2	10.6	10.3	9.8	10.5	10.6	10.4	10.3	10.5	10.5	10.4	10.1	3.6	165

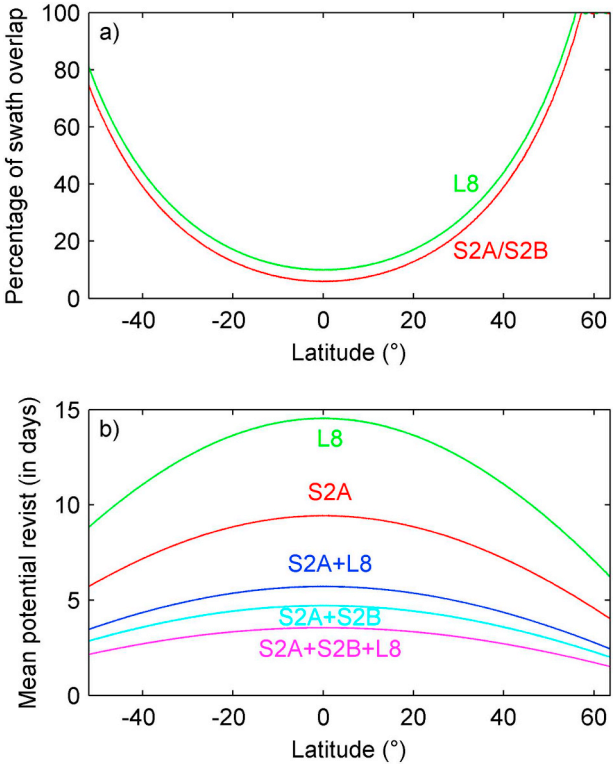

Fig. 6. Percentage of overlap between adjacent orbits (a) and mean potential revisit cycle (b) as a function of the latitude for Landsat 8 (L8), Sentinel-2A (S-2A) and three VC configurations.

presented, relying on retrieved uncertainty for each independent algorithm. Then, emphasis is placed on the product evaluation through three analyses of the products to characterize the overall quality of the HLS data set: (i) cross-comparison with MODIS, (ii) evaluation of the spatial co-registration and (iii) temporal consistency.

5.1. Theoretical uncertainty budget

The theoretical uncertainty budget is computed as the sum of the squares of uncertainty from the component algorithms, obtainable from the literature: (i) atmospheric correction (Vermote et al., 2016) and (ii) BRDF normalization (Roy et al., 2016). The residual error of the polynomial fit (Table 4) is used as the uncertainty of the bandpass adjustment algorithm. Notice that undetected clouds may produce much larger errors that are not accounted in this budget.

The validation of SR products, i.e. of atmospheric correction, has been studied extensively and the protocol of validation is well defined. The core is a comparison of the SR with a simulated SR using TOA reflectance, measured atmospheric characteristics (mostly from the Aerosol Robotic Network) and a radiative transfer model. The uncertainties of the Landsat 8 OLI SR retrieved by Vermote et al. (2016) are reported in Table 6. Notice that the theoretical uncertainties does not account for adjacency effects or terrain effects.

There is no a well-defined protocol for validating the BRDF normalization. However, since the c-factor technique and calibrated coefficients by Roy et al. (2016) were used for the HLS, we can take the absolute differences that Roy et al. computed using adjacent Landsat-5/Landsat-7 swaths (Table 6) as the BRDF normalization uncertainty. Notice that it is not possible to distinguish systematic error from non-systematic error. Moreover, an important assumption is made: the uncertainties were computed using TM and ETM+ data. This statement tends (i) to overestimate the HLS products uncertainty as radiometry resolution of OLI and MSI are higher than TM and ETM+ (Markham et al., 2015), and (ii) to underestimated S10/S30 uncertainty because MSI has a wider field of view than TM or ETM+ (20.6° as compared to 15°).

The theoretical errors of the three HLS products (last 3 columns of Table 6) were deduced using the sum of the squares of the involved processing for each product, assuming independence of each individual error of the three processing steps. The assumption is known to be false, but this approach does not underestimate the uncertainty error. Most of the error is related to the atmospheric correction and the BRDF-normalization processing, while the bandpass-adjustment impacts the overall error by < 1%. The ultra blue, blue and SWIR 2.1 bands display the highest errors due to higher impact of the atmosphere. The BRDF normalization adds about 10% to the error for all bands, except for the blue band; the high TM/ETM+ atmospheric error on blue band is carried over to the BRDF error reported by Roy et al. (2016).

5.2. Cross-comparison with MODIS

The cross-comparison with the MODIS approach has been introduced by Claverie et al. (2015b). The approach consists in comparing HLS surface reflectance (SR) with the validated long-term SR data record from MODIS Terra. The approach includes four major processing steps:

1. Spatial averaging of cloud-free S30/L30 pixels over a coarse resolution MODIS grid (0.05° in latitude and longitude, corresponding to approximatively 5 km).
2. Adjustment of the sun-view geometry (i.e. BRDF) differences between the S30/L30 products (nadir view, constant SZA as defined in Section 3.4) and the MODIS MOD09CMG products. In order to adjust MODIS SR to the sun-view geometry configuration used by the HLS, we use an approach different from the one used in Section 3.4: the VJB method (Vermote et al., 2009) and the associated BRDF database. The good performance of this method as applied to the MODIS CMG product has been proven by several studies (Breon et al., 2015; Breon and Vermote, 2012; Claverie et al., 2015a; Franch et al., 2014), but the coarse spatial resolution of the BRDF database limits the interpretation of the results.
3. Adjustment of the spectral bandpass differences between L30/S30

Table 6
Theoretical uncertainty (σ) budget of the three processing algorithms: (i) atmospheric correction (atm.-correction, from Vermote et al., 2016), (ii) BRDF-normalization (BRDF-norm., from Roy et al., 2016), and bandpass-adjustment (bandpass-adj., from Section 3.6). HLS errors (3 last columns) are provided in absolute values and, under brackets, in relative values by dividing the later by the global L30/S30 means per band.

Spectral band	$\sigma_{atm.\text{-}correction}$	$\sigma_{BRDF\text{-}norm.}$	$\sigma_{bandpass\text{-}adj.}$	σ_{S10}	σ_{S30}	σ_{L30}
Ultra blue	0.0110	–	0.0004	0.011 (33%)	0.011 (33%)	0.011 (33%)
Blue	0.0085	0.0083	0.0018	0.009 (19%)	0.014 (29%)	0.012 (25%)
Green	0.0054	0.0086	0.0011	0.005 (7%)	0.01 (13%)	0.01 (13%)
Red	0.0040	0.0096	0.0015	0.004 (4%)	0.011 (11%)	0.01 (10%)
NIR	0.0026	0.0241	0.0003	0.003 (1%)	0.024 (10%)	0.024 (10%)
SWIR 1.6	0.0011	0.0189	0.0001	0.001 (0%)	0.019 (8%)	0.019 (8%)
SWIR 2.1	0.0036	0.0141	0.0020	0.004 (2%)	0.015 (8%)	0.015 (8%)

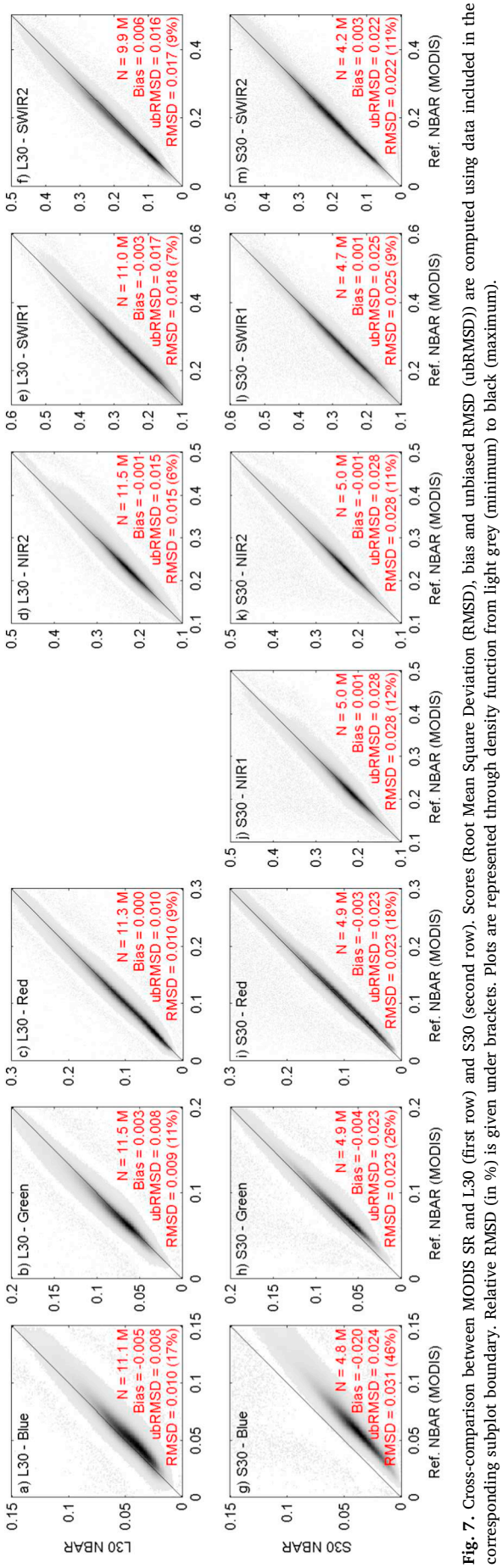

Fig. 7. Cross-comparison between MODIS SR and L30 (first row) and S30 (second row). Scores (Root Mean Square Deviation (RMSD), bias and unbiased RMSD (ubRMSD)) are computed using data included in the corresponding subplot boundary. Relative RMSD (in %) is given under brackets. Plots are represented through density function from light grey (minimum) to black (maximum).

and MODIS. We use a different approach compared to HLS, relying on the Spectral Band Adjustment Factors (SBAF), a spectral ratio to relate two analogue spectral bands (Chander et al., 2013). A look-up-table (LUT) relating SBAF (i.e., ratio between OLI and MODIS reflectances) to MODIS spectra was computed for every Hyperion spectra of the data set mentioned in Section 3.6. For each MODIS observation, a SBAF is retrieved from the LUT using a nearest-neighbor algorithm. The SBAF are finally applied to the MODIS reflectance to adjust for the spectral differences between MODIS and OLI bandpass.

4. Temporal matching. In order to maximize the number of MODIS observations that can be used in cross-comparison, we defined a three-step decision rule: (i) use MODIS data from the same day as HLS if it is valid, otherwise (ii) average valid MODIS ± 1 day, otherwise (iii) average valid MODIS ± 2 days. This rule increases the number of available MODIS valid observations, without modifying the non-systematic error of the overall results. Moreover, the averaging process tends to reduce the variability in MODIS surface reflectance. MODIS pixels are selected if the number mapping of the MOD09CMG products is equal to 0. HLS-aggregated pixels are selected if 99% of the QA layer of the pixels included in the CMG pixel indicates no cloud, no shadow, no cirrus, no snow and no water.

Fig. 7 shows the overall results of the cross-comparison exercise, for data up to June-2017. It appears that some points for the S30 comparison are far from the 1:1 line, probably due to major cloud omission in HLS processing of the Sentinel-2 products. The quality of Fmask applied for Sentinel-2 is likely not optimal, and the lack of thermal data is a major causal factor. Therefore, a procedure to flag and discard products with poor QC results was set up. L30 and S30 Products were flagged if they contain > 1 CMG pixel where $\Delta\rho_{Green}$ (Eq. (5)) is lower than −0.04 or $R\rho_{Green}$ (Eq. (6)) higher than 3. The green band was selected as atmospheric and cloud impacts significantly this domain of the spectra while not being used for AOT retrieval. The thresholds were set manually based on Fig. 7.

$$\Delta\rho_{Green} = \rho_{MODIS,Green} - \rho_{HLS,Green} \quad (5)$$

$$R\rho_{Green} = \rho_{MODIS,Green}/\rho_{HLS,Green} \quad (6)$$

This procedure turned out to discard approximatively 2.8% of S10/S30 products and 0.5% of L30 products. The final data set does not include these discarded products. Overall QC results when flagged products are discarded from the analysis are shown in Fig. 8. It appears that only some isolated points are outside the confidence boundary defined using Eqs. (5) and (6), due to cloud omission, and affecting mostly S30 products. The S30 blue deviate significantly from MODIS (bias of about 30%) which is not the case for L30. Knowing the aerosol retrieval, which is partially based on the blue band, is identical for both products, this results suggests an issue in the calibration or in the HLS processing, specifically the spectral adjustment. Apart from the blue band, no major bias is observed. The RMSDs, not exceeding 11% (except blue band), highlight the very good consistency of the HLS compared with the MOD09CMG product.

5.3. Evaluation of the spatial co-registration

Accurate multi-temporal image-to-image registration is critical for high spatial and temporal resolution data sets, and it is particularly important for VCs, because of the disparity in spatial resolution and angular sampling. Therefore, the HLS QC includes a continuous evaluation of the image co-registration accuracy. The analysis is performed using AROP (Gao et al., 2009) on Level-1 Landsat 8 (L1T) and Sentinel-2 (L1C) products. AROP automatically identifies tie points between the reference image and the warp image based on cross-correlation in the NIR band. The geometric error of the Level-1 warp images is assumed to be the coordinate offset in the tie point pairs.

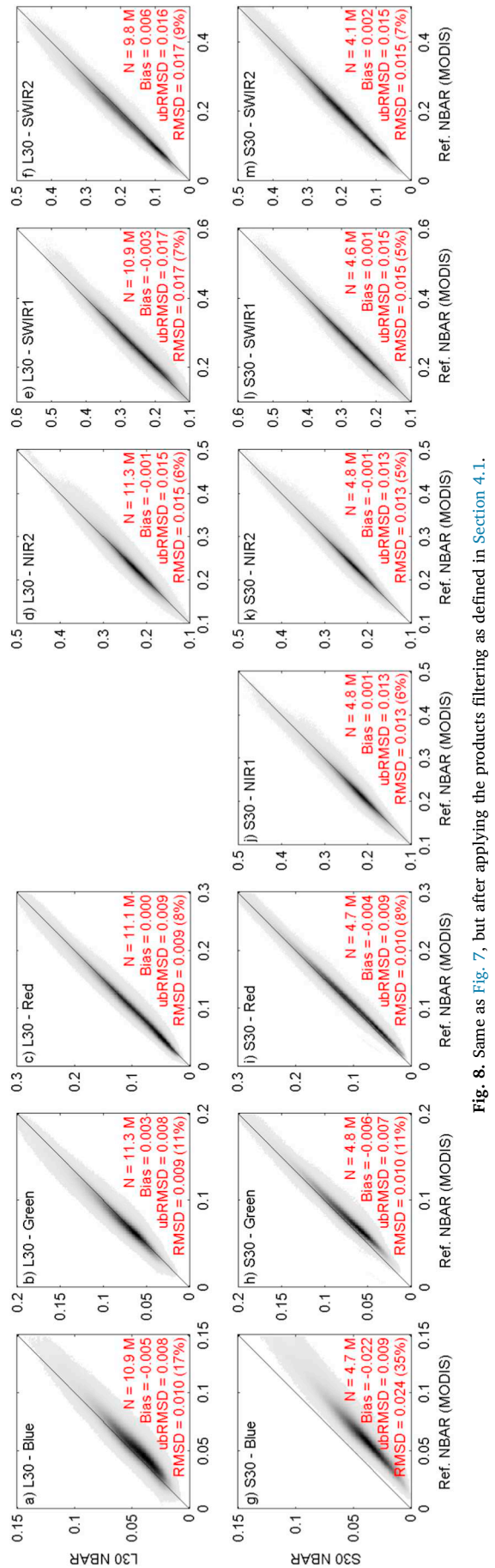

Fig. 8. Same as Fig. 7, but after applying the products filtering as defined in Section 4.1.

This evaluation of the HLS co-registration could not be considered as a validation, since the same algorithm is used for processing and assessing. However, it appears that the overall geometric differences between the reference and warp images are considerably reduced with the use of AROP. We measured a 90% circular error (CE-90, defined as the geometric error of the ninetieth percentile) at 18.8 m and 6.2 m for L30 and S10 products, respectively, corresponding to the same value of 0.62 pixel. It is understandable that AROP failed on about 15% of the products, mostly because the extensive cloud made coverage the identification of tie points impossible in these images. For both L30 and S10 products, the geometric co-registration accuracy is significantly improved over the Level-1 products. The CE90 measured for L1T OLI data (31.5 m) corresponded to 36.4 m (2σ), which is consistent with the finding of Storey et al. (2016, 38 m at 2σ). One can notice on Fig. 9 that Sentinel-2 L1C images from adjacent orbits (L1C-DO) show the higher coordinate offset than L1C images from the same orbits (L1C-SO), confirming the spacecraft yaw integration issue detected on L1C processed with version earlier than v02.04. This pattern is not visible in the S10 products which show a Gaussian distribution of offsets.

5.4. Temporal consistency

The final quality control of the HLS high temporal resolution VC analyzes the time series (TS) consistency through time. We use a TS smoothness index (TSI), defined as an estimate of the time series noise, for three separate TS configurations (S30 + L30, S30, and L30), as in Eq. (7), following the formulation introduced by Vermote et al. (2009).

$$TSI = \sqrt{\frac{\sum_{i=1}^{n-2}\left(y_{i+1} - \frac{y_{i+2}-y_i}{day_{i+2}-day_i} \times (day_{i+i} - day_i) - y_i\right)^2}{N-2}} \quad (7)$$

Given three successive samples of TS ($y_i \ldots y_{i+2}$) of length N measured at day ($day_i \ldots day_{i+2}$), the difference between the center measurement and the linear interpolation of the two exterior measurements quantifies the "noise" of the time series. This estimate thus assumes a local linear variation of surface reflectance between three dates, which can be regarded as realistic throughout the time series except for sharp transitions. We set the threshold of the maximum period between the first and the third sample of the triplets to 20 days for S30 + L30, and to 20 and 32 days for S30 and L30, respectively, corresponding to two repeat cycles. These thresholds correspond to two repeat cycles, allowing 3 observations from the same orbit and up to 5 by combining multiple orbit acquisitions. Note that sharp transitions of surface (e.g., crop/grass harvest, fire) affect the analysis, but their impacts remain limited on TSI since TSI is computed using entire time series. The analysis is performed at full spatial resolution, i.e., 30 m.

Maps of TSI were computed for each tile of the HLS test sites. Fig. 10 shows the red band TSI map of two tiles in South Africa (34HBK, one of the denser cloud-free HLS TS) and in France (31TCJ, dense TS with high amount of cloud). For South Africa, the distribution of TSI is quite homogenous, centered on 0.003 for the configuration L30 + S30. Some dark regions are nonetheless visible on Fig. 10, mostly in configurations using only L30 or S30 TS. They are not impacted by the surface itself, but by some TS outliers due to cloud masking omission, as shown in the sample TS of Fig. 11. They are less visible in the configuration L30 + S30, since the number of triplets increases and, therefore, lower the weight of outliers in the calculation of TSI. Outliers would make the time series analysis difficult for the second tile (31TCJ). While the L30 time series is not significantly affected by outliers, S30 and L30 + S30 are highly contaminated. Because TS outliers mostly correspond to cloud contamination, this TSI observation indicates that S30 cloud masking was less accurate, than the L30 cloud masking. The use of a TS outlier filtering technique allows computation of the TSI, which is directly related to the SR temporal consistency.

The outliers filtering technique used for HLS is a combination of a temporal filter with a spatial filter. The standard median filter, named

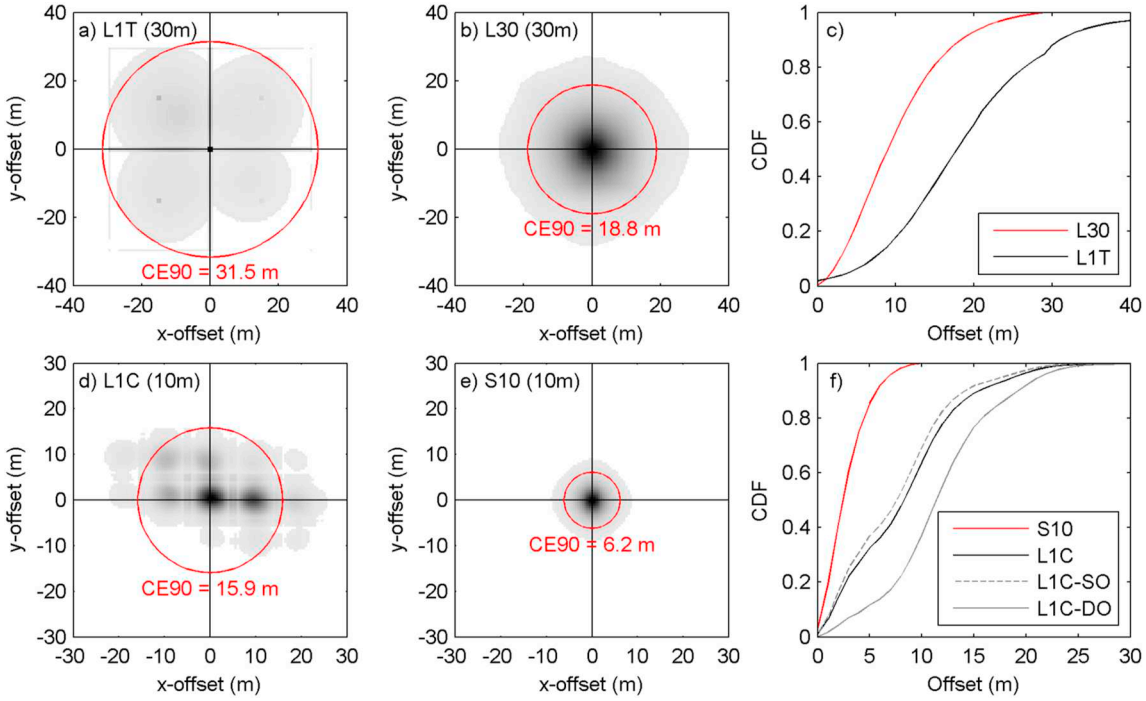

Fig. 9. x and y offsets (in meters) in UTM projection between GCPs from the reference image and corresponding ground control points (GCPs) on Landsat L1T (a) and L30 (b), and Sentinel-2 L1C (d) and S10 (e) images. Subplot (c) and (f) show the cumulative distribution function (CDF) of the offset computed from the Euclidean distance of x and y offsets. In subplot (f), distinctions were made between same orbit (SO, dashed grey line) and different orbit (DO, plain grey line) comparisons. Offsets were computed with AROP using Sentinel-2 L1C with baseline version 02.04 as reference. Spatial co-registration results between pairs of Sentinel-2 L1C with baseline version 02.04 are not shown. 160,000 Landsat 8 scenes and 13,000 Sentinel-2 granules were used, yielding to 105 and 43 million GCPs, respectively. Products with 10 or fewer GCPs were not considered. Plots are represented as a density function from light grey (minimum) to black (maximum). CE-90 represents the Circular Error of the 90th percentile in meters.

the Hampel filter (Pearson, 2002), is used to extract temporal outliers in TS using the Vegetation Index (VI = ρ_{NIR} / ρ_{Red}). For each sample of the TS, the filter computes the median of the VIs in a temporal window, for each sample surrounded by 3 samples on each side (center sample excluded). It also estimates the Scale of Natural Variation (SNV) of each sample by deriving the median of the absolute deviations of the 6 samples from the median. If a sample differs from the median by more than three SNV, it is flagged as an outlier. We set the maximum window width no larger than 60 days on each side (i.e., no filter is applied if fewer than 3 samples fit within 60 days on each side). The Hampel filter is combined with a spatial filter to eliminate isolated filtered pixels that generate a speckle effect. The spatial filter is a simple spatial convolution with a circular kernel of 150 m. Final flagged pixels in TS satisfy the following two rules: (i) the sample value is flagged as an outlier by the Hampel filter, (ii) the majority of the surrounding pixels in the circular kernel are flagged as outliers by the Hampel filter. As illustrated in Fig. 11, the outliers filtering technique is able to remove most of the TS outliers, most likely corresponding to omitted clouds. Notice that the filtering approach is not used to discard pixels in the final data set.

Fig. 12 displays the red band TSI map of the same tiles shown in Fig. 10 but after filtering the data with the described technique. The impact of the filter is significant, mostly for S30 for which cloud mask omission error has been described in Section 4.1. Finally, the probability distribution of the TSI in five spectral bands and based on the whole HLS data set is shown in Fig. 13. The filtering technique decreased significantly the S30 TSI (95th percentile decreased by between 41 and 87%), i.e., the filtered S30 TS became smoother. The decrease is less noticeable for L30 since fewer outliers were present and had to be filtered. In terms of number of samples filtered, Fig. 13(p–r) displays the CDF of the number of triplets. When the whole HLS data set is considered, for S30 and L30, there is no major change with the filtering technique since the decrease ranged between only 9% and 6% respectively. The 90th percentile of the TSI, after filtering and considering the S30 + L30 configuration, does not exceed 0.006 for the three selected visible bands and 0.014 for the NIR and SWIR bands. The values are similar if configuration S30 or L30 is selected. These numbers indicate that overall, the TS are relatively smooth, specifically when considering the combined use of Landsat 8 and Sentinel-2 data.

6. Time series examples

The HLS data set has the potential to support a wide variety of applications requiring high temporal and spatial resolutions optical data. Crop monitoring is maybe the most typical one. The 30-meter resolution is optimal for monitoring crop fields for most parts of the world (Lobell, 2013; Masek et al., 2006; Roy et al., 2014), but can be limiting for some small farming system (Bégué et al., 2018; White and Roy, 2015). The dense time series (80% of the global surface will have a potential revisit period of cloud-free observations of 8.4 days or fewer with the VC L8 + S-2A + S-2B) is adequate for detecting the sharp changes of surface, such as vegetation green-up or crop harvest. Figs. 14 to 16 show three time series examples of single pixels, highlighting the high potential of the HLS data set for crop monitoring at field scale. The dense TS (mostly for the first two examples) allows detection of rapid changes, such as a harvest event in early September 2016 in the New Mexico example (Fig. 15). The third case in France is typical of a cloudy area. While the TS is not as dense as the first two cases, most phenological stages of this double cropping system are clearly identifiable.

7. Conclusion

The Harmonized Landsat and Sentinel-2 (HLS) data set is a unique Virtual Constellation (VC) data set produced by NASA. It is composed of

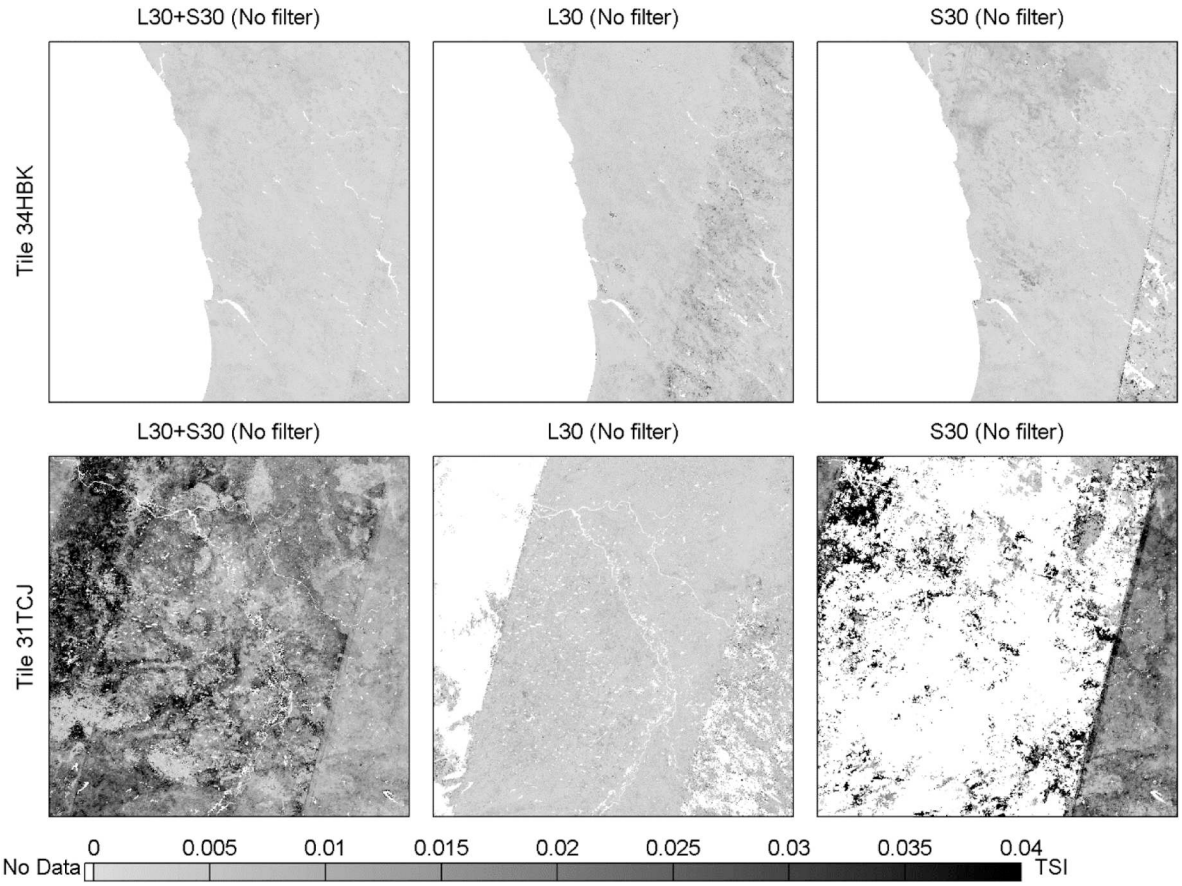

Fig. 10. Red band TSI map of tile 34HBK (South Africa, top row), and tile 31TCJ (France, bottom row). TSI was computed using three TS configurations: (i) considering S30 and L30 together, (ii) L30 alone and (iii) S30 alone. TSI is displayed per pixel using a colormap from light grey (0) to black (0.04). TSI values computed with less than five triplets were filtered out and appear in white.

three products: (i) S10, the full spatial resolution MSI surface reflectance; (ii) S30, the 30 m MSI Nadir BRDF-Adjusted Reflectance (NBAR); and (iii) L30, the 30 m OLI NBAR. It builds on the two recent medium spatial resolution optical satellite missions (Landsat 8 and Sentinel-2) to produce a unified data set, in which all images are easily "stackable". As a result, the HLS VC is a valuable source of data for building a "data cube" to analyze any given pixel through time using data from Landsat 8/OLI and Sentinel-2/MSI seamlessly.

A series of pre-processing steps are applied to obtain a harmonized surface reflectance data set. The core HLS processing step is the atmospheric correction. Both sources of input data, Landsat 8 and Sentinle-2, are processed from TOA reflectance to surface reflectance with the same algorithm, LaSRC, a state-of-the-art atmospheric correction algorithm (Vermote et al., 2016). At present, LaSRC does not correct for adjacency effects since it requires a proper validation framework to be established, which will be part of the further activities within the ACIX initiative (Doxani et al., 2018). In the current HLS v1.3 data, the cloud and cloud-shadow masking for OLI is performed by LaSRC internally, and for MSI by an adapted version of Fmask. The three HLS products are gridded to a common grid, projection, and spatial extent, in the UTM Military Grid Reference System (MGRS) used by Sentinel-2 L1C products. To improve the co-registration (i) between Landsat 8 and Sentinel-2 (Storey et al., 2016), and (ii) within the Sentinel-2 data set, the Automated Registration and Orthorectification Package (Gao et al., 2009) was employed. S30 and L30 HLS products are delivered as NBAR, obtained using the c-factor technique combined with a global constant set of coefficients (Roy et al., 2016). To account for small spectral responses between the two sensors, a bandpass adjustment is applied to S30 products (from MSI) to match the OLI spectral responses.

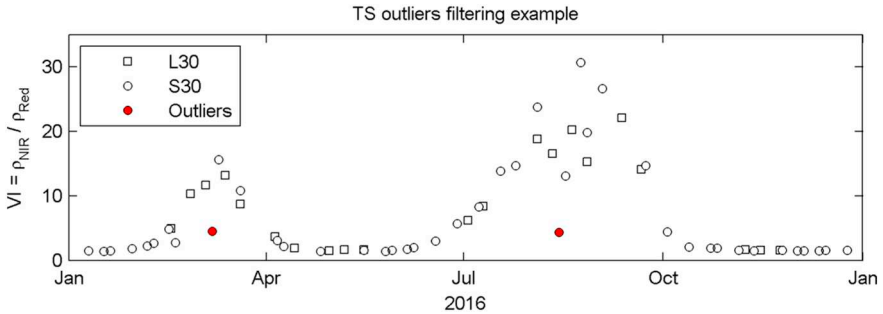

Fig. 11. Example of TS outlier filtering, using the VI TS of pixel within a crop field located in South Africa (32.255°S, 13.448°W). Computed TSIs for this VI TS are 2.28 and 2.98 with filtering and without filtering, respectively.

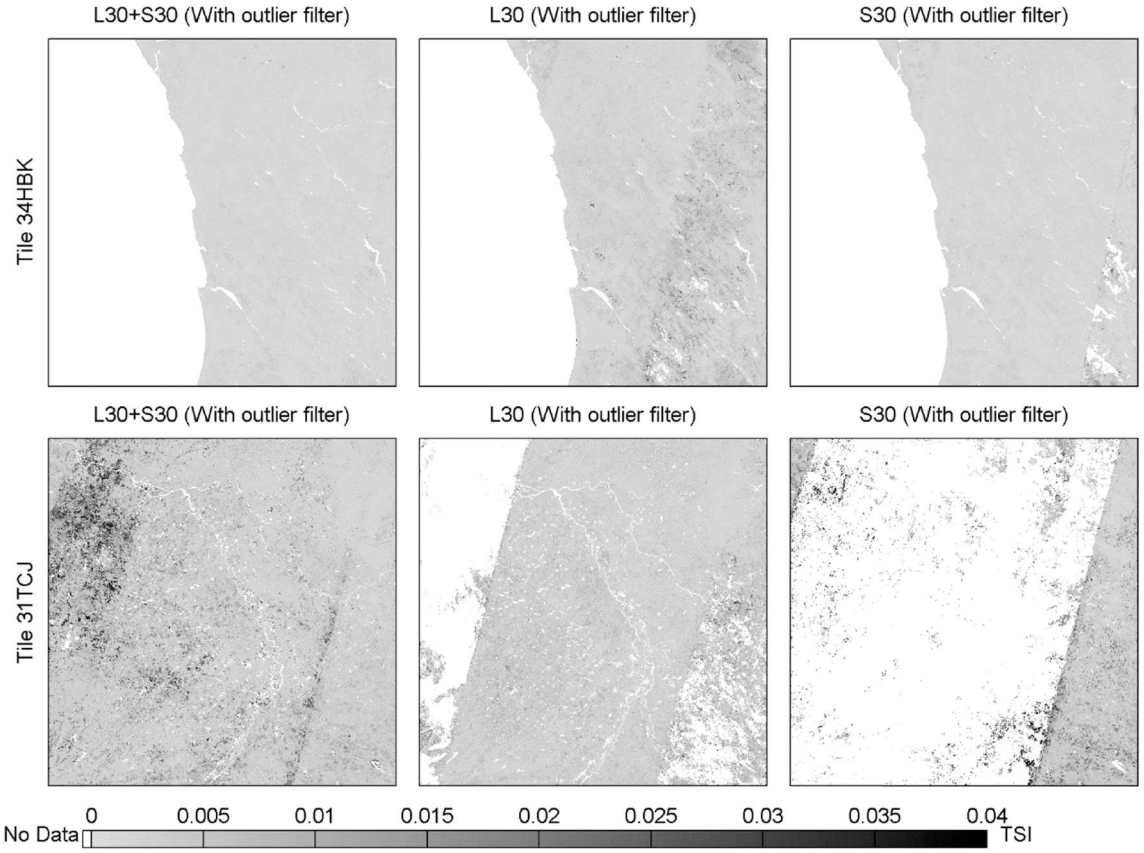

Fig. 12. Same as Fig. 10 but after filtering the TS.

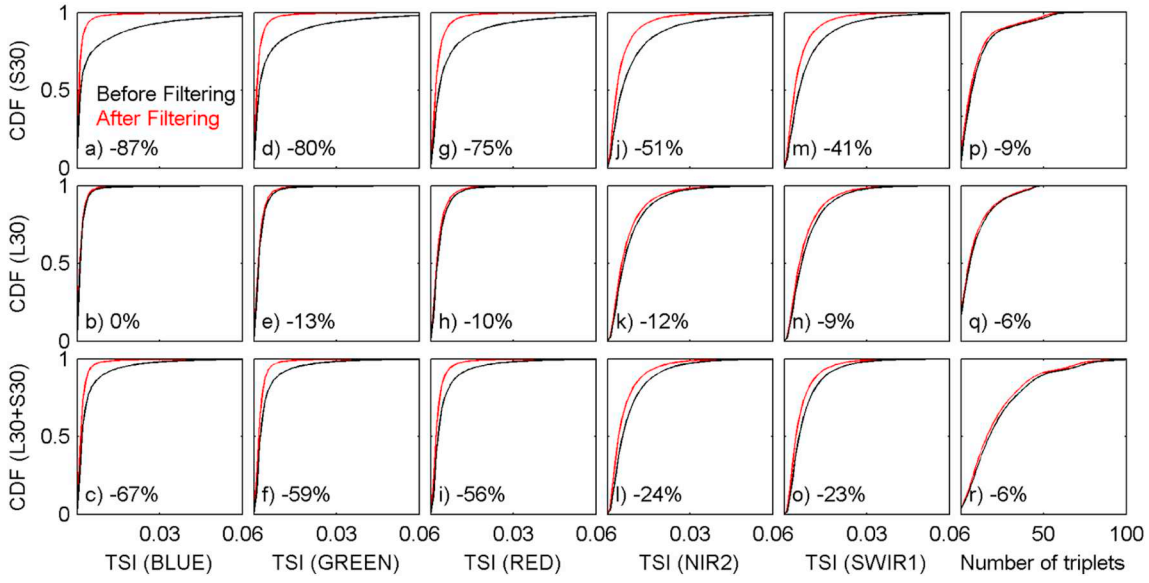

Fig. 13. TSI cumulative distribution functions (CDFs) for the 783 tiles and one year (2016) of data from the HLS data set before (black) and after (red) filtering, considering three configurations (S30, L30 and L30 + S30) and for five selected spectral bands. CDFs of the number of triplets used per TS to compute TSI is displayed in the last column (p–r). Percentages in the bottom left correspond to the change of the 95th percentile from before to after filtering. (For interpretation of the references to color in this figure legend, the reader is referred to the web version of this article.)

As a prototype for a global data set, the HLS v1.3 data set covers about 7.3% of the global terrestrial lands. The prototype locations include the ones requested by users to support specific applications, as well as the ones for reflectance intercomparison with Aeronet and SURFAD. The data set includes some entire countries (Germany, South Africa, Tanzania, and Belgium), large regions (Southeast Australia), and isolated groups of tiles. The temporal coverage of the HLS data set starts with the Landsat 8 launch (spring 2013) and extends to present time.

Product quality control is conducted with a cross-comparison between S30/L30 products and MODIS MCD09CMG products following the methodology introduced in Claverie et al. (2015b). The results show a good overall consistency between the two products. Apart from the

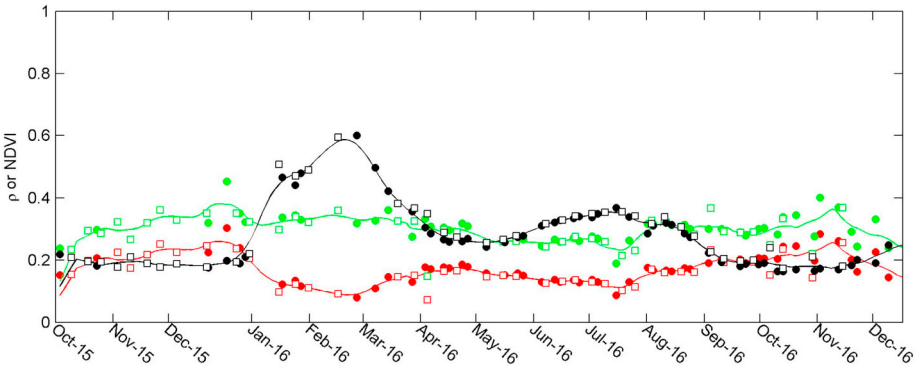

Fig. 14. S30/L30 time series of red SR (red), NIR SR (green) and NDVI (black) of one pixel located at 27.4995°S, 27.285°E (South Africa, tile 35JNK) from Oct-15 to Jan-17. Filled discs and open squares are used for S30 (Sentinel-2) and L30 (Landsat 8), respectively. Lines correspond to a simple convolution of the TS. Outliers were filtered using the technique described in Section 3.4. (For interpretation of the references to color in this figure legend, the reader is referred to the web version of this article.)

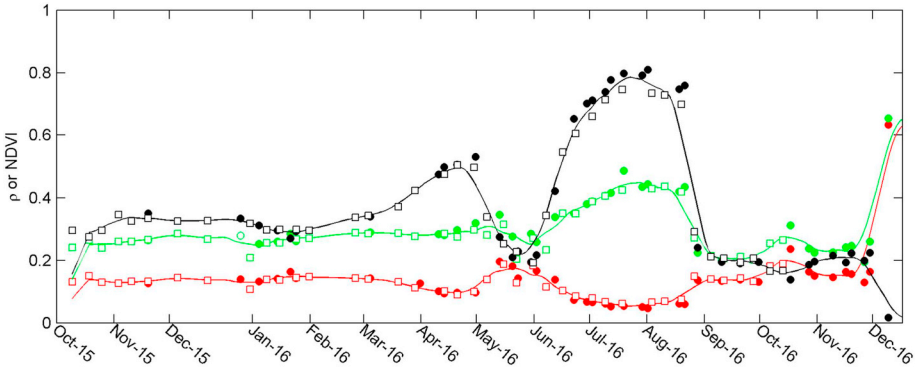

Fig. 15. Same as Fig. 14 for location 34.7806°N, 106.7504°W (New Mexico, USA, tile 13SCU).

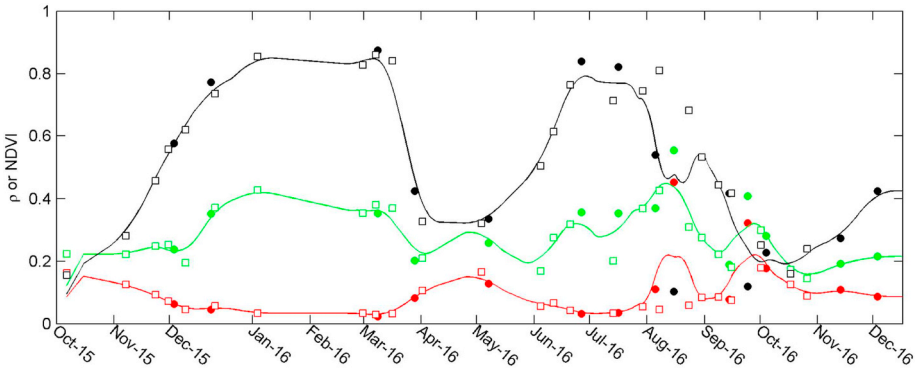

Fig. 16. Same as Fig. 14 for location 43.8137°N, 1.2462°E (France, tile 31TCJ).

blue band, which serves as an atmospheric correction calibrator, the overall relative uncertainties and biases do not exceed 11% and 7% for S30 and L30, respectively. The geometric co-registration error in Level-1 products is reduced by about 40% and 60% during HLS processing of OLI and MSI, respectively. The CE-90 are 6.2 m and 18.8 m, for S10 and L30, respectively. Finally, the time series (TS) smoothness of the data set showed the 90th percentile of the TSI noise does not exceed 0.006 for the visible bands and 0.014 for the NIR and SWIR bands.

The Sentinel-2 cloud mask remains a main known issue for the HLS v1.3 data set. The cross-comparison with MODIS helped to flag some products that are highly affected by clouds. Our time series outlier filtering approach helps considerably to eliminate outliers (mostly residual cloud) from time series. While such filters are promising, one can notice that real surface changes can be mistaken for outliers. Therefore, reliable cloud masking for individual images is critical as a first step. For the next release of HLS data set, we will use the latest version of LaSRC for Sentinel-2 which has cloud masking capability, and this may improve the cloud masking to the level of satisfaction as with Landsat 8. We are also investigating into the potential of other cloud and cloud-shadow detection techniques in the time domain, such as MACCS/MAJA (Hagolle et al., 2010) and Tmask (Zhu and Woodcock, 2014). These algorithms show promise for cloud masking even in the absence of thermal-infrared observations, but require regular cloud free observations of each pixel (better than monthly), for optimal cloud detection.

The HLS project offers to the scientific community and the wider community of remote sensing users a unique free and easy-to-use data set. While the current data set only covers a limited part of the globe, HLS spatial coverage is constantly growing. A wall-to-wall North America HLS data set is planned for release of the version 1.4 in mid-2018, and a global product may follow afterwards. The data set will be processed on a near-real-time basis, including data from Sentinel-2B. Moreover, the v1.4 HLS data set will account for the modified MSI Relative Spectral Response functions (v3.0, published in December 2017). The current v.13 data set is accessible through a public HTTPS interface at https://hls.gsfc.nasa.gov/, and also available on the NASA Earth Exchange (NEX) computing facility.

Acknowledgements

Funding for HLS was provided by NASA through the Land Cover Science Project Office and the Land Cover/Land Use Change Program. The HLS data set contains modified Copernicus Sentinel data (from 2015 to 2017), processed by ESA. The European Space Agency and Copernicus program management and staff, and the USGS Landsat program management and staff, are thanked for the free provision of the Sentinel-2 and Landsat-8 data respectively. We would like to thank John Dwyer (US Geological Survey) for useful discussions regarding data access and processing. We are also grateful to the working teams that supported the implementation of their algorithm: Dr. Feng Gao team (US Department of Agriculture), Dr. Curtis Woodcock team (Boston University) and Dr. David Roy team (South Dakota State University).

References

Becker-Reshef, I., Justice, C., Sullivan, M., Vermote, E., Tucker, C., Anyamba, A., Small, J., Pak, E., Masuoka, E., Schmaltz, J., Hansen, M., Pittman, K., Birkett, C., Williams, D., Reynolds, C., Doorn, B., 2010. Monitoring global croplands with coarse resolution earth observations: the Global Agriculture Monitoring (GLAM) project. Remote Sens. 2, 1589–1609.

Bégué, A., Arvor, D., Bellon, B., Betbeder, J., de Abelleyra, D., Ferraz, R., Lebourgeois, V., Lelong, C., Simões, M., Verón, S.R., 2018. Remote sensing and cropping practices: a review. Remote Sens. 10.

Breon, F.-M., Vermote, E., 2012. Correction of MODIS surface reflectance time series for BRDF effects. Remote Sens. Environ. 125, 1–9.

Breon, F., Vermote, E., Murphy, E., Franch, B., 2015. Measuring the directional variations of land surface reflectance from MODIS. IEEE Trans. Geosci. Remote Sens. 1–12.

CEOS, 2016. CEOS Analysis Ready Data for Land (CARD4L) Description Document.

Chander, G., Mishra, N., Helder, D.L., Aaron, D.B., Angal, A., Choi, T., Xiong, X., Doelling, D.R., 2013. Applications of spectral band adjustment factors (SBAF) for cross-calibration. IEEE Trans. Geosci. Remote Sens. 51, 1267–1281.

Claverie, M., Demarez, V., Duchemin, B., Hagolle, O., Ducrot, D., Marais-Sicre, C., Dejoux, J.-F., Huc, M., Keravec, P., Beziat, P., Fieuzal, R., Ceschia, E., Dedieu, G., 2012. Maize and sunflower biomass estimation in southwest France using high spatial and temporal resolution remote sensing data. Remote Sens. Environ. 124.

Claverie, M., Vermote, E., Franch, B., He, T., Hagolle, O., Kadiri, M., Masek, J., 2015a. Evaluation of medium spatial resolution BRDF-adjustment techniques using multi-angular SPOT4 (Take5) acquisitions. Remote Sens. 7, 12057.

Claverie, M., Vermote, E., Franch, B., Masek, J., 2015b. Evaluation of the Landsat-5 TM and Landsat-7 ETM + surface reflectance products. Remote Sens. Environ. 169, 390–403.

Dechoz, C., Poulain, V., Massera, S., Languille, F., Greslou, D., de Lussy, F., Gaudel, A., L'Helguen, C., Picard, C., Tremas, T., 2015. Sentinel 2 global reference image. In: Conference on Image and Signal Processing for Remote Sensing XXI. Toulouse, France.

Doxani, G., Vermote, E., Roger, J.-C., Gascon, F., Adriaensen, S., Frantz, D., Hagolle, O., Hollstein, A., Kirches, G., Li, F., Louis, J., Mangin, A., Pahlevan, N., Pflug, B., Vanhellemont, Q., 2018. Atmospheric correction inter-comparison exercise. Remote Sens. 10 (2), 352.

Drusch, M., Del Bello, U., Carlier, S., Colin, O., Fernandez, V., Gascon, F., Hoersch, B., Isola, C., Laberinti, P., Martimort, P., Meygret, A., Spoto, F., Sy, O., Marchese, F., Bargellini, P., 2012. Sentinel-2: ESA's optical high-resolution mission for GMES operational services. Remote Sens. Environ. 120, 25–36.

Egorov, V.A., Roy, P.D., Zhang, K.H., Hansen, C.M., Kommareddy, A., 2018. Demonstration of percent tree cover mapping using Landsat analysis ready data (ARD) and sensitivity with respect to Landsat ARD processing level. Remote Sens. 10.

ESA, 2015. Sentinel-2 User Handbook.

ESA, 2018. Data Quality Report S2-PDGS-MPC-DQR.

Foga, S., Scaramuzza, P.L., Guo, S., Zhu, Z., Dilley, R.D., Beckmann, T., Schmidt, G.L., Dwyer, J.L., Hughes, M.J., Laue, B., 2017. Cloud detection algorithm comparison and validation for operational Landsat data products. Remote Sens. Environ. 194, 379–390.

Franch, B., Vermote, E.F., Claverie, M., 2014. Intercomparison of Landsat albedo retrieval techniques and evaluation against in situ measurements across the US SURFRAD network. Remote Sens. Environ. 152, 627–637.

Gao, F., Masek, J.G., Wolfe, R.E., 2009. Automated registration and orthorectification package for Landsat and Landsat-like data processing. J. Appl. Remote. Sens. 3.

Gao, F., He, T., Masek, J.G., Shuai, Y., Schaaf, C.B., Wang, Z., 2014. Angular effects and correction for medium resolution sensors to support crop monitoring. IEEE J. Sel. Top. Appl. Earth Obs. Remote Sens. 7, 4480–4489.

Gascon, F., Bouzinac, C., Thépaut, O., Jung, M., Francesconi, B., Louis, J., Lonjou, V., Lafrance, B., Massera, S., Gaudel-Vacaresse, A., 2017. Copernicus Sentinel-2A calibration and products validation status. Remote Sens. 9, 584.

Gorelick, N., Hancher, M., Dixon, M., Ilyushchenko, S., Thau, D., Moore, R., 2017. Google Earth Engine: planetary-scale geospatial analysis for everyone. Remote Sens. Environ. 202, 18–27.

Hagolle, O., Huc, M., Pascual, D.V., Dedieu, G., 2010. A multi-temporal method for cloud detection, applied to FORMOSAT-2, VENμS, LANDSAT and SENTINEL-2 images. Remote Sens. Environ. 114, 1747–1755.

Hall, D.K., Riggs, G.A., Salomonson, V.V., DiGirolamo, N.E., Bayr, K.J., 2002. MODIS snow-cover products. Remote Sens. Environ. 83, 181–194.

Hansen, M.C., Loveland, T.R., 2012. A review of large area monitoring of land cover change using Landsat data. Remote Sens. Environ. 122, 66–74.

Hansen, M., DeFries, R., Townshend, J.R.G., Sohlberg, R., 1998. UMD Global Land Cover Classification, 1 Kilometer, 1981–1994, 1.0. U.o.M. Department of Geography, College Park, Maryland.

Ju, J., Roy, D.P., Vermote, E., Masek, J., Kovalskyy, V., 2012. Continental-scale validation of MODIS-based and LEDAPS Landsat ETM plus atmospheric correction methods. Remote Sens. Environ. 122, 175–184.

Justice, C., Gutman, G., Vadrevu, K.P., 2015. NASA Land Cover and Land Use Change (LCLUC): an interdisciplinary research program. J. Environ. Manag. 148, 4–9.

Kotchenova, S.Y., Vermote, E.F., 2007. Validation of a vector version of the 6S radiative transfer code for atmospheric correction of satellite data. Part II. Homogeneous Lambertian and anisotropic surfaces. Appl. Opt. 46, 4455–4464.

Languille, F., Dechoz, C., Gaudel, A., Greslou, D., de Lussy, F., Tremas, T., Poulain, V., 2015. Sentinel 2 geometric image quality commissioning - first results. In: Conference on Image and Signal Processing for Remote Sensing XXI. Toulouse, France.

Li, J., Roy, D., 2017. A global analysis of Sentinel-2A, Sentinel-2B and Landsat-8 data revisit intervals and implications for terrestrial monitoring. Remote Sens. 9, 902.

Lobell, D.B., 2013. The use of satellite data for crop yield gap analysis. Field Crop Res. 143, 56–64.

Louis, J., Debaecker, V., Pflug, B., Main-Knorn, M., Bieniarz, J., Mueller-Wilm, U., Cadau, E., Gascon, F., 2016. SENTINEL-2 SEN2COR: L2A processor for users. In: Ouwehand, L. (Ed.), ESA Living Planet Symposium 2016. Spacebooks Online, pp. 1–8.

Loveland, T.R., Dwyer, J.L., 2012. Landsat: building a strong future. Remote Sens. Environ. 122, 22–29.

Markham, B.L., Barsi, J.A., Kaita, E., Ong, L., Morfitt, R., Haque, M.O., 2015. Radiometric calibration and stability of the Landsat-8 Operational Land Imager (OLI). In: Conference on Earth Observing Systems XX. San Diego, CA.

Martimort, P., Berger, M., Curnicero, B., Del Bello, U., Fernandez, V., Gascon, F., Silvestrin, P., Spoto, F., Sy, O., 2007. Sentinel-2 - The Optical High-resolution Mission for GMES Operational Services. Esa Bulletin-European Space Agency, pp. 18–23.

Masek, J.G., Vermote, E.F., Saleous, N.E., Wolfe, R., Hall, F.G., Huemmrich, K.F., Gao, F., Kutler, J., Lim, T.K., 2006. A Landsat surface reflectance dataset for North America, 1990–2000. IEEE Geosci. Remote Sens. Lett. 3, 68–72.

Melaas, E.K., Friedl, M.A., Zhu, Z., 2013. Detecting interannual variation in deciduous broadleaf forest phenology using Landsat TM/ETM plus data. Remote Sens. Environ. 132, 176–185.

Middleton, E.M., Ungar, S.G., Mandl, D.J., Ong, L., Frye, S.W., Campbell, P.E., Landis, D.R., Young, J.P., Pollack, N.H., 2013. The earth observing one (EO-1) satellite mission: over a decade in space. IEEE J. Sel. Top. Appl. Earth Obs. Remote Sens. 6, 243–256.

Montanaro, M., Gerace, A., Lunsford, A., Reuter, D., 2014. Stray light artifacts in imagery from the Landsat 8 thermal infrared sensor. Remote Sens. 6, 10435–10456.

Nemani, R., 2011. NASA Earth Exchange: next generation earth science collaborative. In: Isprs Bhopal 2011 Workshop Earth Observation for Terrestrial Ecosystem. vol. 38-8. pp. 17.

Pearson, R.K., 2002. Outliers in process modeling and identification. IEEE Trans. Control Syst. Technol. 10, 55–63.

Roy, D.P., Borak, J.S., Devadiga, S., Wolfe, R.E., Zheng, M., Descloitres, J., 2002. The MODIS land product quality assessment approach. Remote Sens. Environ. 83, 62–76.

Roy, D.P., Lewis, P., Schaaf, C.B., Devadiga, S., Boschetti, L., 2006. The global impact of clouds on the production of MODIS bidirectional reflectance model-based composites for terrestrial monitoring. IEEE Geosci. Remote Sens. Lett. 3, 452–456.

Roy, D.P., Ju, J., Lewis, P., Schaaf, C., Gao, F., Hansen, M., Lindquist, E., 2008. Multi-temporal MODIS-Landsat data fusion for relative radiometric normalization, gap filling, and prediction of Landsat data. Remote Sens. Environ. 112, 3112–3130.

Roy, D.P., Ju, J.C., Kline, K., Scaramuzza, P.L., Kovalskyy, V., Hansen, M., Loveland, T.R., Vermote, E., Zhang, C.S., 2010. Web-enabled Landsat Data (WELD): Landsat ETM plus composited mosaics of the conterminous United States. Remote Sens. Environ. 114, 35–49.

Roy, D.P., Wulder, M.A., Loveland, T.R., Woodcock, C.E., Allen, R.G., Anderson, M.C., Helder, D., Irons, J.R., Johnson, D.M., Kennedy, R., Scambos, T., Schaaf, C.B., Schott, J.R., Sheng, Y., Vermote, E.F., Belward, A.S., Bindschadler, R., Cohen, W.B., Gao, F., Hipple, J.D., Hostert, P., Huntington, J., Justice, C.O., Kilic, A., Kovalskyy, V., Lee, Z.P., Lymbumer, L., Masek, J.G., McCorkel, J., Shuai, Y., Trezza, R., Vogelmann, J., Wynne, R.H., Zhu, Z., 2014. Landsat-8: science and product vision for terrestrial global change research. Remote Sens. Environ. 145, 154–172.

Roy, D.P., Zhang, H.K., Ju, J., Gomez-Dans, J.L., Lewis, P.E., Schaaf, C.B., Sun, Q., Li, J., Huang, H., Kovalskyy, V., 2016. A general method to normalize Landsat reflectance data to nadir BRDF adjusted reflectance. Remote Sens. Environ. 176, 255–271.

Roy, D.P., Li, J., Zhang, H.K., Yan, L., Huang, H., Li, Z., 2017. Examination of Sentinel-2A multi-spectral instrument (MSI) reflectance anisotropy and the suitability of a general method to normalize MSI reflectance to nadir BRDF adjusted reflectance. Remote Sens. Environ. 199, 25–38.

Shelestov, A., Lavreniuk, M., Kussul, N., Novikov, A., Skakun, S., 2017. Exploring Google Earth engine platform for Big Data Processing: classification of multi-temporal satellite imagery for crop mapping. Front. Earth Sci. 5, 17.

Skakun, S., Kussul, N., Shelestov, A., Kussul, O., 2014. Flood hazard and flood risk assessment using a time series of satellite images: a case study in Namibia. Risk Anal. 34, 1521–1537.

Skakun, S., Roger, J.-C., Vermote, E.F., Masek, J.G., Justice, C.O., 2017a. Automatic sub-pixel co-registration of Landsat-8 Operational Land Imager and Sentinel-2A Multi-

Spectral Instrument images using phase correlation and machine learning based mapping. Int. J. Digital Earth 1–17.
Skakun, S., Vermote, E., Roger, J.C., Franch, B., 2017b. Combined use of Landsat-8 and Sentinel-2A images for winter crop mapping and winter wheat yield assessment at regional scale. AIMS Geosci. 3, 163–186.
Storey, J., Choate, M., Lee, K., 2014. Landsat 8 operational land imager on-orbit geometric calibration and performance. Remote Sens. 6, 11127–11152.
Storey, J., Roy, D.P., Masek, J., Gascon, F., Dwyer, J., Choate, M., 2016. A note on the temporary misregistration of Landsat-8 Operational Land Imager (OLI) and Sentinel-2 Multi Spectral Instrument (MSI) imagery. Remote Sens. Environ. 186, 121–122.
Strahler, A.H., Lucht, W., Schaaf, C.B., Tsang, T., Gao, F., Li, X., Lewis, P., Barnsley, M., 1999. In: Documentation, M. (Ed.), MODIS BRDF/Albedo Product: Algorithm Theoretical Basis Document Version 5.0, (Boston).
Teillet, P.M., Fedosejevs, G., Thome, K.J., Barker, J.L., 2007. Impacts of spectral band difference effects on radiometric cross-calibration between satellite sensors in the solar-reflective spectral domain. Remote Sens. Environ. 110, 393–409.
Trinh, R.C., Fichot, C.G., Gierach, M.M., Holt, B., Malakar, N.K., Hulley, G., Smith, J., 2017. Application of Landsat 8 for monitoring impacts of wastewater discharge on coastal water quality. Front. Mar. Sci. 4.
USGS, 2018. Landsat Analysis Ready Data (ARD).
Vermote, E.F., Kotchenova, S., 2008. Atmospheric correction for the monitoring of land surfaces. J. Geophys. Res.-Atmos. 113.
Vermote, E., Saleous, N., 2007. LEDAPS Surface Reflectance Product Description.
Vermote, E., Justice, C.O., Breon, F.-M., 2009. Towards a generalized approach for correction of the BRDF effect in MODIS directional reflectances. IEEE Trans. Geosci. Remote Sens. 47.
Vermote, E., Justice, C., Claverie, M., Franch, B., 2016. Preliminary analysis of the performance of the Landsat 8/OLI land surface reflectance product. Remote Sens. Environ. 185, 46–56.
Waldner, F., De Abelleyra, D., Veron, S.R., Zhang, M., Wu, B.F., Plotnikov, D., Bartalev, S., Lavreniuk, M., Skakun, S., Kussul, N., Le Maire, G., Dupuy, S., Jarvis, I., Defourny, P., 2016. Towards a set of agrosystem-specific cropland mapping methods to address the global cropland diversity. Int. J. Remote Sens. 37, 3196–3231.
Whitcraft, A.K., Becker-Reshef, I., Justice, C.O., 2015a. A framework for defining spatially explicit earth observation requirements for a global agricultural monitoring initiative (GEOGLAM). Remote Sens. 7, 1461–1481.
Whitcraft, A.K., Vemiote, E.F., Becker-Reshef, I., Justice, C.O., 2015b. Cloud cover throughout the agricultural growing season: impacts on passive optical earth observations. Remote Sens. Environ. 156, 438–447.
White, E.V., Roy, D.P., 2015. A Contemporary Decennial Examination of Changing Agricultural Field Sizes Using Landsat Time Series Data.
Woodcock, C.E., Allen, R., Anderson, M., Belward, A., Bindschadler, R., Cohen, W., Gao, F., Goward, S.N., Helder, D., Helmer, E., Nemani, R., Oreopoulos, L., Schott, J., Thenkabail, P.S., Vermote, E.F., Vogelmann, J., Wulder, M.A., Wynne, R., 2008. Free access to Landsat imagery. Science 320, 1011.
Wulder, M.A., Masek, J.G., Cohen, W.B., Loveland, T.R., Woodcock, C.E., 2012. Opening the archive: how free data has enabled the science and monitoring promise of Landsat. Remote Sens. Environ. 122, 2–10.
Yan, L., Roy, D.P., Li, Z., Zhang, H.K., Huang, H., 2018. Sentinel-2A multi-temporal misregistration characterization and an orbit-based sub-pixel registration methodology. Remote Sens. Environ. 215, 495–506.
Zhang, H.K., Roy, D.P., Kovalskyy, V., 2016. Optimal solar geometry definition for global long-term Landsat time-series bidirectional reflectance normalization. IEEE Trans. Geosci. Remote Sens. 54, 1410–1418.
Zhang, H.K., Roy, D.P., Yan, L., Li, Z., Huang, H., Vermote, E., Skakun, S., Roger, J.-C., 2018. Characterization of Sentinel-2A and Landsat-8 top of atmosphere, surface, and nadir BRDF adjusted reflectance and NDVI differences. Remote Sens. Environ. 215, 482–494.
Zhu, Z., Woodcock, C.E., 2012. Object-based cloud and cloud shadow detection in Landsat imagery. Remote Sens. Environ. 118, 83–94.
Zhu, Z., Woodcock, C.E., 2014. Automated cloud, cloud shadow, and snow detection in multitemporal Landsat data: an algorithm designed specifically for monitoring land cover change. Remote Sens. Environ. 152, 217–234.
Zhu, Z., Wang, S., Woodcock, C.E., 2015. Improvement and expansion of the Fmask algorithm: cloud, cloud shadow, and snow detection for Landsats 4-7, 8, and Sentinel 2 images. Remote Sens. Environ. 159, 269–277.